Available online at www.sciencedirect.com

ScienceDirect

Geochimica et Cosmochimica Acta 253 (2019) 63–83

Geochimica et Cosmochimica Acta

www.elsevier.com/locate/gca

Phosphorous incorporation in olivine crystallized from potassium-rich magmas

Özlem Ersoy [a,*], Igor K. Nikogosian [a,b], Manfred J. van Bergen [a], Paul R.D. Mason [a]

[a] Department of Earth Sciences, Utrecht University, Princetonlaan 8A, 3584 CB Utrecht, the Netherlands
[b] Department of Earth Sciences, Vrije Universiteit, Amsterdam, the Netherlands

Received 14 June 2018; accepted in revised form 7 March 2019; Available online 18 March 2019

Abstract

Olivine phenocrysts in basaltic rocks carry valuable mineral-chemical information on early evolution processes in mafic magmatic systems. Fast intra-crystalline diffusion and re-equilibration weakens this potential for major cation constituents of olivine, but the relative immobility of phosphorous makes this element a promising tracer of early crystallization histories. Although phosphorous zoning patterns and underlying kinetic controls have been studied in recent years, little is known about compositional controls on phosphorous incorporation into igneous olivines. We have analysed olivine phenocrysts, hosting Mg-rich melt inclusions, from a range of mafic potassium-rich lavas from Quaternary volcanic centres in Italy for phosphorous and associated trace elements by laser ablation inductively coupled mass spectrometry (LA-ICP-MS), and intra-crystal zoning by electron probe micro-analysis (EPMA) using Kα X-ray elemental maps and quantitative traverses. The studied olivines are marked by low and variable phosphorous concentrations (generally $\leq$ 200 ppm, but up to 435 ppm in enriched zones). In most cases, phosphorous zoning is decoupled from zoning in any other element or forsterite content. From a comprehensive database of melt inclusions and host phenocrysts, we infer that the composition of the host melt (silica and phosphorous activities) and olivine crystallization dynamics (interplay between diffusion rate of cation constituents in the melt and crystal growth rate) largely regulate phosphorous incorporation in olivines. Melt composition is likely the most important control under near-equilibrium crystallization conditions, as apparent phosphorous partition coefficients tend to increase with increasing silica activity. A negative relationship between apparent partition coefficients and $X_{PO2.5}$ indicates that phosphorous partitioning into olivine may deviate from Henry's law behaviour. Melt inclusions are virtually always surrounded by phosphorous-poor zones that are also depleted in Cr and enriched in Al and Ti, suggesting that supply-limited slow growth and coupled-substitution mechanisms largely govern phosphorous uptake here. Our results demonstrate the potential versatility of phosphorous as sensitive indicator of crystal-growth histories and magmatic evolution processes in mafic systems.

Keywords: Olivine; Phosphorous; Zoning; Potassic magmas; Italy

1. INTRODUCTION

Forsterite-rich olivine, usually the first major phase to crystallize from basaltic magma, potentially hosts valuable information about early melt evolution, crystallization and the dynamics of volcanic plumbing systems. The crystallization history of olivine phenocrysts may be recorded as zoning, but their original compositional make-up is often lost due to fast diffusion of divalent cations (e.g., Fe-Mg, Ni) under magmatic conditions, facilitated by the relatively simple structure and composition of the mineral (e.g., Coogan et al., 2005; Dohmen et al., 2007; Chakraborty,

* Corresponding author.
E-mail address: S.R.Chaneva@uu.nl (Ö. Ersoy).

https://doi.org/10.1016/j.gca.2019.03.012
0016-7037/

2010; Spandler and O'Neill, 2010). Phosphorous is a promising new tracer to decipher early crystallization histories of basaltic magma systems since it is one of the highly incompatible trace elements that can be measured in olivine using readily available analytical techniques (Witt-Eickschen and O'Neill, 2005; Batanova et al., 2015), as well as one of the slowest diffusing elements in silicate minerals (Spandler et al., 2007; Spandler and O'Neill, 2010; Watson et al., 2015). To date, P zoning has been described in olivines from (1) ocean island basalts (e.g., Milman-Barris et al., 2008; Welsch et al., 2013, 2014; Shea et al., 2015), (2) igneous cumulates (e.g., Welsch et al., 2014; Xing et al., 2017), (3) mantle xenoliths (e.g., Mallmann et al., 2009; Baziotis et al., 2017), and (4) meteorites (e.g., McCanta et al., 2009, 2016; Li et al., 2017) and partitioning of P into igneous olivine has been discussed in several studies (e.g., Brunet and Chazot, 2001; Foley et al., 2011; Grant and Kohn, 2013; Baziotis et al., 2017). Currently, little is known about the control of bulk composition on P uptake by olivines in alkaline systems. Grant and Kohn (2013) used a synthetic Fe-free trachyandesitic composition to show that melt structure is one of the factors controlling the partitioning of P into olivine.

Zoning of P in olivines is universal and usually rather complex (Welsch et al., 2014). It may correlate with zoning in other cations such as Al^{3+} and Cr^{3+} in olivines from subalkaline basalts, komatiites and meteorites (Milman-Barris et al., 2008; Hofmann, 2010), Li^{+} and Na^{+} in mantle olivines (Mallmann et al., 2009) or show no relationships with other cations (Foley et al., 2011). Experimental studies on the formation of phosphoran olivine indicate that P^{5+} substitutes for Si^{4+} in the tetrahedral site and that charge balance is maintained by octahedral vacancies (Boesenberg and Hewins, 2010). From spatially corresponding zoning and positive correlations in element concentrations, coupled substitutions with trivalent (e.g., Al^{3+}, Cr^{3+}) or monovalent cations (e.g., Na^{+}, Li^{+}) that enter the octahedral site have also been proposed (Milman-Barris et al., 2008; Mallmann et al., 2009).

Phosphorous concentrations in magmatic olivines are highly variable, reaching 925 ppm in subalkaline basalts from Hawaii (Milman-Barris et al., 2008), whilst Ugandan potassic rocks contain up to 83 ppm (Foley et al., 2011) and Gorgona komatiites hardly exceed 200 ppm (Milman-Barris et al., 2008; Hofmann, 2010). Mantle olivines may contain up to 650 ppm P (Brunet and Chazot, 2001; Mallmann et al., 2009), and secondary olivines in veined composite mantle xenoliths up to 2700 ppm P (Baziotis et al., 2017). Considering that the Hawaiian magma contained only 0.16 wt.% (Milman-Barris et al., 2008) and Ugandan potassic rocks up to 0.45 wt.% P_2O_5 (Foley et al., 2011), P concentrations of magmas are apparently not directly reflected in those of the olivines they produce. Recent studies (Foley et al., 2011, 2013) have pointed out that the olivine-liquid partitioning behaviour of some trace elements (e.g., Ni, Co, Cr, Ti) in alkaline melts may differ from that in basaltic melts. For example, the partition coefficient for Ni can be up to six times higher, and for Ti slightly lower in alkaline melts (Foley et al., 2013). These findings, in combination with observed contrasts in P concentrations in olivines crystallized from basaltic and potassic melts, make melt composition effects on partitioning of P into olivine conceivable, which calls for a comprehensive test.

Olivine crystallization experiments yielded P partition coefficients in the range of 0.02–0.5 for ferrobasaltic (Toplis et al., 1994), 0.04–0.05 for nepheline basanitic (Adam and Green, 2006), 0.04–0.69 for basaltic (Milman-Barris et al., 2008), 0.03–0.18 for komatiitic (Hofmann, 2010), and 0.05–1.41 for Fe-free trachyandesitic melts (Grant and Kohn, 2013). Partition coefficients reported for natural terrestrial mineral-melt pairs are in the range of 0.019–0.055 for alkaline to subalkaline basalt and subalkaline andesite basalt (Anderson and Greenland, 1969), 0.1 for spinel lherzolite (Brunet and Chazot, 2001), 0.01–0.02 for ugandite and leucite basanite (Foley et al., 2011), and 0.03–0.28 for composite xenoliths composed of lherzolite, websterite, dunite and orthopyroxenite layers (Baziotis et al., 2017). The high variability in the partition coefficients reported for different melt systems may be indicative of a melt-composition control on partitioning of P into olivine.

Partition coefficients of P between olivine and melt reported for terrestrial rocks partially overlap the experimental data and fall in the range of 0.01–0.28, insufficiently low to account for concentrations reported for P-enriched zones in magmatic olivines and phosphoran olivines (e.g., Milman-Barris et al., 2008). Relatively rapid crystal growth (Milman-Barris et al., 2008) and fast cooling through high temperatures (Boesenberg et al., 2004; Boesenberg and Hewins, 2010) have been proposed as mechanisms responsible for the formation of P-enriched and phosphoran olivine, respectively. Welsch et al. (2013, 2014) proposed rapid, diffusion controlled dendritic olivine growth and subsequent overgrowth and infilling as mechanisms responsible for formation of various P zoning patterns observed in igneous olivines. In addition, metasomatism by a P-rich fluid or melt has been suggested as the mechanism responsible for formation of P-enriched and phosphoran olivine in mantle and meteoritic olivines (Mallmann et al., 2009; Li et al., 2017).

In this study, we investigated the incorporation and zoning patterns of P and associated trace elements (e.g., Al, Cr, Ti) in igneous olivines, focusing on K-rich mafic volcanic rocks with a wide range of P contents, alkali enrichment and degree of silica undersaturation. Samples were collected from an array of Quaternary volcanic centres across peninsular Italy that produced a large compositional spectrum of mantle-derived magmas with variable degrees of K enrichment (Conticelli et al., 2010; Peccerillo, 2017). Our comprehensive data-set, including averaged concentrations determined by LA-ICP-MS across a large number of samples and higher spatial resolution EPMA data for selected samples, aimed at exploring systematics in the uptake of P by olivine, complements existing results from experiments and natural volcanic rocks that have been largely devoted to subalkaline rock types so far. We discuss apparent P partitioning behaviour using P concentrations determined in forsteritic olivines and their Mg-rich melt inclusions (MI), intra-crystal zoning patterns and relationships with other trace elements for a variety of melt compositions.

Table 1
Major element compositions of the studied samples (XRF) and ranges of Fo contents of olivine phenocrysts hosting MI (EPMA). Numbers of olivine phenocrysts and MI analyzed in each sample are given in brackets next to sample names. KAM: Kamafugitic series, HKS: High-K series, SHO: Shoshonitic series, HKCA: High-K calcalkaline series, CA: Calcalkaline series. Magmatic provinces and rock-series classification according to Peccerillo (2005).

Magmatic province	Magmatic Centers	Series	Samples	Locations	Whole Rock Major Oxides (wt.%)											Host olivines
					SiO_2	TiO_2	Al_2O_3	Fe_2O_3[c]	MnO	MgO	CaO	Na_2O	K_2O	P_2O_5	Total[g]	Fo (mol.%)[d]
Intra-Apennine	San Venanzo	KAM	SV (18[a]:12[b])	Pian di Celle	41.82	0.79	10.39	7.57	0.13	12.56	15.69	1.10	7.73	0.41	98.19	88.9–92.5
Roman Province	ColliAlbani	HKS	Alb-1 (7:10)	Villa Senni eruption	46.16	0.81	17.61	9.14	0.19	3.83	9.29	2.65	8.36	0.59	98.62	85.3–90.1
	Sabatini	HKS	Sab-5 (13:23)	Monte Maggiore quarry	48.58	0.71	14.12	7.92	0.14	6.75	11.27	1.40	7.27	0.40	98.55	90.3–91.8
	Vulsini	HKS	Vul-1(1:2)	Bolsena	46.83	0.78	13.74	8.20	0.14	7.31	13.95	1.27	6.03	0.39	98.64	89.5
			Vul-9 (1:1)	Bolsena	49.28	0.82	15.53	7.77	0.14	7.21	11.42	1.52	5.13	0.36	99.17	82.9
			Vul-10 (2:3)	Montefiascone	47.80	0.69	12.37	7.48	0.15	9.16	17.06	1.17	3.17	0.24	99.28	89.7–90.4
			Vul-11 (2:3)	Montefiascone	47.34	0.68	12.48	7.50	0.13	11.83	15.30	1.28	3.15	0.25	99.95	90.9–91.0
			Vul-14 (6:7)	Montefiascone	45.58	0.75	12.63	8.53	0.14	8.76	13.89	1.02	6.30	0.42	98.00	88.4–89.9
	Latera[e]	HKS	Lat-18 (2:4)	East Valentano	47.44	0.99	17.61	9.29	0.16	4.70	11.29	2.41	3.70	0.50	98.09	86.3–87.2
		SHO	Lat-20 (4:2)	Selva del Lamone lava flow	54.95	0.74	16.79	6.38	0.12	5.82	8.35	2.83	4.36	0.20	100.54	89.3–90.2
			Lat-22 (3:4)	Selva del Lamone lava flow	54.58	0.75	16.10	6.36	0.13	5.21	8.27	2.84	4.56	0.21	99.01	89.2–90.1
			Lat-23 (2:3)	Selva del Lamone lava flow	54.61	0.77	16.84	6.57	0.12	5.32	8.59	2.76	4.46	0.21	100.25	89.1–89.4
			Lat-24 (2:2)	Selva del Lamone lava flow	55.34	0.74	16.90	6.32	0.12	4.81	7.57	2.85	4.61	0.19	99.45	88.7–89.5
Ernici-Roccamonfina	Ernici[f]	HKS	Ern-4 (9:11)	Pofi	48.30	0.79	17.71	8.04	0.15	4.46	10.83	2.60	7.47	0.47	100.81	88.3–90.0
			Ern-5 (1:1)	Giuliano di Roma	47.77	0.84	16.35	8.38	0.15	5.74	11.84	2.74	6.64	0.39	100.84	89.3
		CA	Ern-6 (9:12)	Colle Spinazzeta	49.97	0.77	16.25	8.42	0.15	6.94	13.13	4.32	0.61	0.26	100.84	88.1–89.5
	Roccamonfina[f]	HKS	Rocc-7 (17:17)	Masseria Robetti	46.88	0.95	14.95	9.19	0.15	6.78	13.16	1.86	6.44	0.56	100.92	86.7–90.4
		SHO	Rocc-5 (6:6)	Sipicciano	51.40	0.96	17.73	9.27	0.15	5.09	10.71	2.13	3.21	0.28	100.93	86.3–90.5
			Rocc-8 (3:4)	Monte Atano	48.34	0.93	17.10	9.98	0.16	7.02	13.31	1.89	1.99	0.28	101.00	86.6–89.3
		HKCA	Rocc-6 (10:7)	Masseria Robetti	48.19	0.88	18.21	10.13	0.17	6.74	12.87	2.06	1.41	0.34	101.01	87.6–91.3
Campania	Somma-Vesuvius	HKS	Ves-2 (18:28)	Ranieri quarry 1834 lava flow	47.88	1.03	15.70	8.57	0.15	5.73	11.44	2.17	6.02	0.80	99.48	81.7–90.1
	Campi Flegrei	SHO	CF (6:11)	Academia	59.51	0.57	18.26	4.82	0.14	1.49	3.95	3.20	8.41	0.19	100.52	86.7–89.3
Vulture	Vulture	HKS	Melf-4 (1:0)	Carier	44.29	1.17	16.56	8.58	0.19	5.06	11.42	4.39	3.68	1.01	96.36	87.5
			Melf-7 (23:32)	Fogianno	46.08	1.51	14.88	8.42	0.14	6.60	11.90	3.46	4.11	1.07	98.17	82.2–89.5
			Melf-9 (4:3)	Carier	44.66	1.31	17.34	8.91	0.19	4.56	11.49	3.09	4.58	0.92	97.05	87.3–88.1

[a] Number of analyzed olivine grains.
[b] Number of analyzed MI.
[c] All iron expressed as Fe_2O_3.
[d] Fo (mol.%) = [Mg/(Mg + Fe)].
[e] Whole rock major oxide data published in Nikogosian et al. (2016).
[f] Whole rock major oxide data published in Nikogosian and van Bergen (2010).
[g] Deviations of totals from 100% reflects additional volatile components which were not measured here.

2. SAMPLES

Samples were obtained from 10 Quaternary volcanic centres distributed across peninsular Italy from Latera in the north to Vulture in the south (Table 1, Fig. 1a). They represent relatively unevolved mafic lavas (MgO > 4 wt.% with the exception of Colli Albani and Campi Flegrei samples), spanning a wide compositional range that covers Calc-alkaline (CA), high-K Calc-alkaline (HKCA) and shoshonitic (SHO) basalts, as well as ultrapotassic leucite-bearing high-K series (HKS) and kamafugitic (KAM) rock types (Conticelli et al., 2010; Peccerillo, 2017). For consistency with previous literature, we use the nomenclature of K-rich rocks as described by Peccerillo (2005, 2017).

Olivines hosting melt inclusions were separated from crushed rocks. Melt inclusions were homogenized and analysed for major, minor, and trace element concentrations following sample preparation and experimental procedures as described in Nikogosian and van Bergen (2010). Melt inclusion data for Roccamonfina-Ernici and Latera samples have been previously published in Nikogosian and Van Bergen (2010) and Nikogosian et al. (2016). Olivines and their MIs were first analysed by EPMA for their major element contents. From the olivines 163 crystals were selected for Laser Ablation Inductively Coupled Mass Spectrometry (LA-ICP-MS) analysis. With a few exceptions, the olivines are the most forsteritic in each lava sample, while their MIs reflect variability in P_2O_5, K_2O and volatile contents. Based on P concentrations determined by LA-ICP-MS, 33 olivine crystals were selected for high-precision electron microprobe analysis (EPMA) to investigate intracrystal variations of P from rim-to-rim, core-to-rim, and MI-to-rim transects with 5–20 μm spacing depending on the size of the crystals. The selected olivines span the range from highest to lowest forsterite and P concentrations for each sample. Based on the EPMA transects, six olivine grains were further selected for high resolution elemental mapping by EPMA using Wavelength-Dispersive Spectrometry (WDS).

3. ANALYTICAL PROCEDURES AND METHODS

Whole-rock compositions of the samples were determined with a Philips PW1404/10 XRF at the Free University, Amsterdam following standard techniques. USGS reference materials AVG-1, BCR-2, BHVO-2, and GSP-1 were analysed together with the unknown samples to monitor data quality. Precision was better than 5% relative (2 SD) for all elements. Melt inclusions in the most forsteritic olivines were selected for re-homogenization experiments using a high-T heating/quenching stage (Sobolev et al., 1980) at the Free University, Amsterdam, according to experimental procedures described in Danyushevsky et al. (2002b) and Nikogosian et al. (2002). Homogenized MI were analysed for major and trace element concentrations by EPMA with a JEOL JXA8600 Superprobe at Utrecht University, following methods and techniques described in De Hoog et al. (2001). Natural minerals, metals and synthetic oxides were used as calibration standards.

Phosphorous concentrations along with other minor and trace elements were determined in olivine by LA-ICP-MS using a GeoLas 200Q Excimer laser ablation system (193 nm wavelength) coupled to a Thermo Finnigan Element 2 sector field ICP-MS instrument, operated in low-resolution mode. Analyses were performed by ablation of polished olivine separates embedded in epoxy, using a constant fluence of 5 J cm^{-2}, and pulse repetition rate of

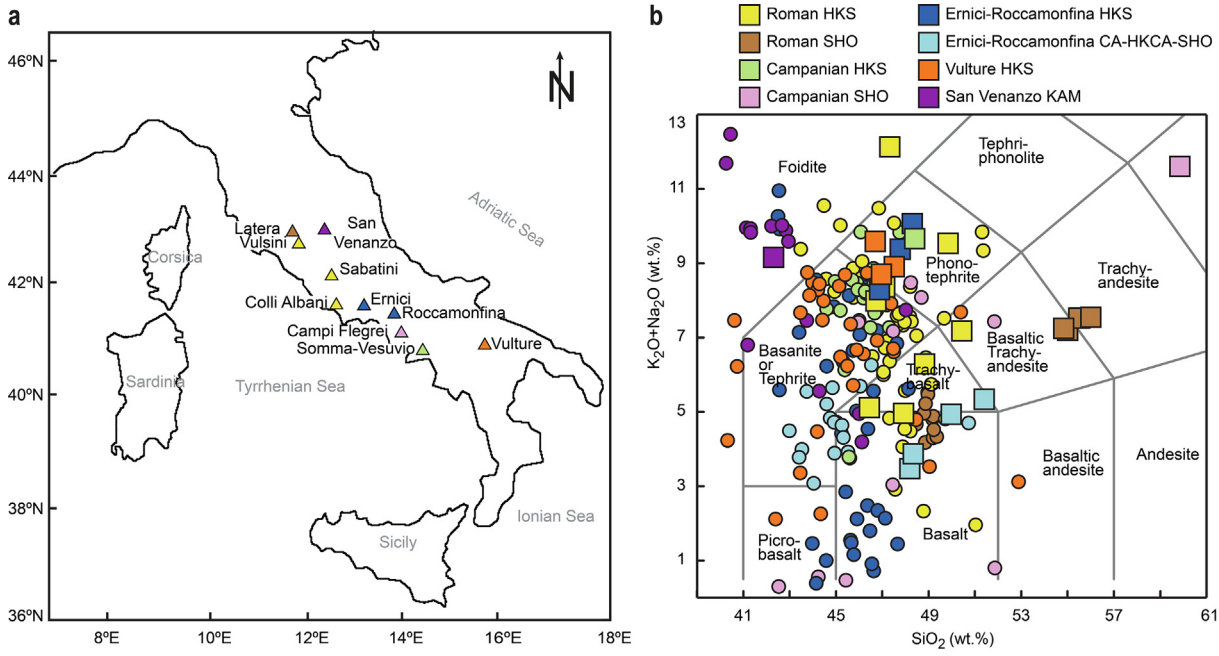

Fig. 1. (a) Location of volcanic centres samples collected from. Map redrawn after Peccerillo (2017). (b) Total alkali versus silica diagram (Le Maitre et al., 2002) for the studied rock samples (squares) and melt inclusions (circles).

5 Hz to produce 80 μm diameter craters for reaching acceptable detection limits. Silicon, determined by electron microprobe analysis, was used as an internal standard element, and NIST SRM 610 glass (Pearce et al., 1997) was used as the calibration standard. Accuracy and precision were monitored by repetitive analysis of international reference glasses ATHO-Ga (Jochum et al., 2006), USNM 111240/52 VG-2 (Jarosewich et al., 1980), and NIST SRM 612 (Pearce et al., 1997) (Supplementary Table 1), selected primarily for the range of their P contents being similar to that expected for olivines. Background count rates were measured for 30 s prior to and after ablation of the olivines for 60 s. The time resolved signal was continuously monitored during ablation to ensure that no subsurface inclusions or cracks were included in an analysis.

Measured isotopes included ^{7}Li, ^{23}Na, ^{27}Al, ^{29}Si, ^{31}P, ^{43}Ca, ^{49}Ti, ^{53}Cr, ^{55}Mn, ^{57}Fe, and ^{60}Ni. Trace element concentrations in measured reference glasses generally fell within the uncertainty limits of certified values (Jarosewich et al., 1980; Pearce et al., 1997; Jochum et al., 2006), except for Al and Fe (ATHO-Ga) that were within 5 % relative, and Ti (ATHO-Ga and USNM 111240/52 VG-2), Na (NIST SRM 612), Ca and P (USNM 111240/52 VG-2) that were within 10 % relative of the certified values. Ni measured in ATHO-Ga showed larger deviations from the certified value but was in excellent agreement with the data published by Canil et al. (2003). Limits of quantification (LOQ) for each analysis point were calculated as ten times the standard deviation on the gas blank signal. Concentrations lower than LOQ are not reported.

Electron microprobe analyses of the olivines were performed with a JEOL JXA-8600 Superprobe equipped with five wavelength-dispersive spectrometers at Utrecht University. An accelerating voltage of 15 kV and beam current of 100 nA with 1 μm beam diameter were used for spot analyses and traverses. Phosphorous, Al, Si, Mg were analysed on TAP, Ca and Ti on PETJ, Cr and Mn on PET, and Fe and Ni on the LIF crystals. In-house standards corundum (Al), diopside (Ca), hematite (Fe), tephroite (Mn), Cr_2O_3 (Cr), rutile (Ti) and potassium titanyl phosphate ($KTiPO_5$) (P) were used for calibration. Si and Mg were calibrated against San Carlos olivine (USNM 111312/44). Peak counting times were 30 s for Si, Fe, Mg; 70 s for Ca, Mn; 120 s for Cr, Ti; 160 s for Al, Ni, and P, and background counting times were half the peak counting time at two background positions for each element. A φ(ρz) algorithm supplied by NORAN SERIES II automation software was utilized for matrix correction. Five to ten points in San Carlos olivine (USNM 111312/44) were analysed between each batch of 20–30 olivine measurements to monitor instrumental drift (Table 2). Oxide sums of 100 ± 2 wt. % and cations sums of 3.00 ± 0.02 per four oxygens were used for quality assessment of olivine data, and any results that did not comply were discarded. The analytical conditions resulted in a typical detection limit and 2 SD error of 22 and 12 ppm for P, 14 and 8 ppm for Al, 49 and 16 ppm for Ti, 57 and 16 ppm for Cr, based on counting statistics.

Table 2
EPMA data for the San Carlos olivine standard (USNM# 111312/44). Reference values for major oxides are certified values (Jarosewich et al., 1980) and reference values for trace elements are the averages of 49 analyses from Gurenko et al. (2010).

	San Carlos olivine (USNM# 111312/44)	
	Certified/Reference	This study (n = 444)
Fo (mol.%)[a]	90	89.90 ± 0.25
SiO_2 (wt.%)	40.81	40.58 ± 0.25
MgO (wt.%)	49.42	49.41 ± 0.34
FeO (wt.%)[b]	9.55	9.90 ± 0.09
MnO (wt.%)	0.14	0.12 ± 0.003
NiO (wt.%)	0.37	0.37 ± 0.007
Ca (ppm)	651 ± 63	656 ± 25
Al (ppm)	161 ± 18	150 ± 10
Cr (ppm)	90 ± 8	64 ± 15

[a] Fo (mol.%) = [Mg/(Mg + Fe)].
[b] All iron expressed as FeO.

Kα x-ray intensity maps of P, Al, Cr, Ca, Si, Mg, Fe, Mn, and Ni were acquired using JEOL JXA-8530F Hyperprobe Field Emission Electron probe microanalyser at Utrecht University. Five maps were acquired simultaneously for P, Al, Cr and Ca. Phosphorous was analysed both with a TAPH and a PETH crystal simultaneously but only PETH images are reported in this study due to improved counting statistics using the PETH crystal. Al was analysed with a high intensity TAPH, Cr with a large PETL, and Ca with high intensity PETH crystals. An accelerating voltage of 15 kV and beam current of 400 nA was used with a focused beam of 1 μm diameter. Dwell time per pixel was 500 ms and step size was 1 μm for each map resulting in total acquisition times from 35 to 108 h corresponding to mapped areas of 0.25–0.78 mm^2. Beam current variation was less than 1.7% throughout all mapping sessions. Si, Mg, Fe, Mn and Ni were mapped in a separate session with 15 kV accelerating voltage, 100 nA beam current, 1 μm beam diameter, 100 ms dwell times and 1 μm step size.

4. RESULTS

Olivine compositions from LA-ICP-MS spot analyses are given in Supplementary Table 2, and average EPMA compositions are given in Table 3. From here onwards, the P concentrations in olivines are reported as ppm P and those in MI and bulk rock samples as wt.% P_2O_5.

4.1. Phosphorous concentration in olivines and olivine-hosted melt inclusions

Phosphorous concentrations in olivines from the Italian potassic rocks that we investigated here were relatively low, reaching a maximum of 435 ppm in enriched zones based on the EPMA transects, but generally not exceeding 200 ppm according to the LA-ICP-MS spot analysis. Melt inclusions hosted by olivine phenocrysts (Fo_{82}-Fo_{93}) contained 0.16–1.91 wt.% P_2O_5. The P contents of both the olivines and the MI were highly variable in most of

Table 3
Average compositions of the olivines determined by EPMA transects in each phenocryst. The standard deviations are calculated from all analyzed points with higher than detection limit concentrations per given element in each olivine, and reflect the compositional heterogeneity in each olivine phenocryst. Standard errors based on EPMA counting statistics are given in Section 3.

Sample	Olivine Code	N[a]	Fo (mol.%)[b]	SiO_2 (wt.%)	MgO (wt.%)	CaO (wt.%)	FeO (wt.%)[c]	MnO (wt.%)	NiO (wt.%)	Ti (ppm)	Al (ppm)	Cr (ppm)	P (ppm)	nTi[d]	nCr[e]	nP[f]
Alb-1	36	79	85.63 ± 0.30	39.67 ± 0.17	46.24 ± 0.32	0.71 ± 0.03	13.83 ± 0.25	0.34 ± 0.01	0.14 ± 0.01	62 ± 14	58 ± 28	<dl[g]	94 ± 59	36		76
Alb-1	81	126	90.66 ± 0.16	40.43 ± 0.15	50.04 ± 0.27	0.54 ± 0.03	9.19 ± 0.14	0.16 ± 0.00	0.18 ± 0.01	59 ± 8	85 ± 19	123 ± 21	40 ± 11	22	125	107
Sab-5	14	136	90.45 ± 1.99	40.56 ± 0.30	50.17 ± 1.66	0.47 ± 0.05	9.42 ± 1.76	0.16 ± 0.03	0.21 ± 0.01	53 ± 17	89 ± 24	221 ± 39	155 ± 80	10		129
Sab-5	22	127	90.41 ± 0.67	40.38 ± 0.21	49.12 ± 0.52	0.46 ± 0.07	9.29 ± 0.62	0.15 ± 0.01	0.19 ± 0.01	60 ± 9	92 ± 31	183 ± 30	125 ± 72	34		121
Vul-10	55	106	90.82 ± 0.23	41.02 ± 0.19	50.71 ± 0.34	0.39 ± 0.04	9.13 ± 0.21	0.14 ± 0.01	0.22 ± 0.01	61 ± 17	109 ± 12	212 ± 28	48 ± 15	10		83
Vul-14	57	86	89.54 ± 0.32	40.52 ± 0.22	49.20 ± 0.24	0.67 ± 0.08	10.24 ± 0.31	0.20 ± 0.03	0.21 ± 0.01	55 ± 5	79 ± 12	111 ± 38	44 ± 13	10	68	71
Lat-18	42	242	87.81 ± 0.23	39.86 ± 0.26	48.26 ± 0.42	0.38 ± 0.03	11.94 ± 0.19	0.19 ± 0.00	0.16 ± 0.01	55 ± 8	107 ± 34	76 ± 12	51 ± 20	38	187	216
Lat-22	26	70	90.33 ± 0.35	40.16 ± 0.11	50.17 ± 0.27	0.30 ± 0.01	9.57 ± 0.34	0.14 ± 0.01	0.28 ± 0.01	51 ± 13	184 ± 15	266 ± 44	42 ± 12	8		64
Lat-23	158	147	89.19 ± 0.34	40.52 ± 0.14	49.04 ± 0.34	0.29 ± 0.01	10.60 ± 0.31	0.15 ± 0.01	0.27 ± 0.01	57 ± 9	195 ± 27	245 ± 45	56 ± 27	14		109
Ern-6	16	107	88.62 ± 0.45	40.08 ± 0.16	49.02 ± 0.46	0.29 ± 0.02	11.22 ± 0.39	0.16 ± 0.01	0.16 ± 0.01	60 ± 12	70 ± 14	101 ± 17	26 ± 3	12	102	9
Ern-6	158	119	88.52 ± 0.83	40.16 ± 0.25	48.70 ± 0.68	0.30 ± 0.08	11.25 ± 0.77	0.16 ± 0.02	0.18 ± 0.02	62 ± 15	96 ± 57	141 ± 40	62 ± 25	36	111	41
Rocc-7	136	85	87.77 ± 0.14	40.47 ± 0.14	48.28 ± 0.18	0.47 ± 0.02	11.99 ± 0.13	0.21 ± 0.00	0.17 ± 0.01	63 ± 13	98 ± 16	58	54 ± 31	37	1	64
Rocc-7	271	27	88.63 ± 0.04	40.59 ± 0.09	48.72 ± 0.11	0.48 ± 0.00	11.14 ± 0.04	0.17 ± 0.00	0.15 ± 0.01	55 ± 34	90 ± 25	<dl	56 ± 16			
Rocc-8	145	73	88.42 ± 0.90	40.06 ± 0.23	48.82 ± 0.67	0.26 ± 0.02	11.39 ± 0.86	0.17 ± 0.02	0.18 ± 0.01	55 ± 9	66 ± 30	187 ± 128	29 ± 4	3		10
Rocc-6	76	123	91.31 ± 0.17	40.80 ± 0.16	50.90 ± 0.25	0.29 ± 0.04	8.63 ± 0.17	0.14 ± 0.01	0.22 ± 0.01	54 ± 4	75 ± 14	260 ± 27	35 ± 8	2		53
Rocc-6	80	71	89.40 ± 0.14	40.32 ± 0.16	49.59 ± 0.20	0.32 ± 0.01	10.48 ± 0.14	0.16 ± 0.00	0.14 ± 0.01	63 ± 12	87 ± 16	79 ± 14	35 ± 8	29	55	35
Ves-2L	130	108	87.41 ± 0.91	40.42 ± 0.32	47.88 ± 0.82	0.36 ± 0.04	12.29 ± 0.82	0.21 ± 0.02	0.17 ± 0.01	61 ± 14	66 ± 14	111 ± 28	86 ± 43	27	89	104
Ves-2b	18	105	89.55 ± 1.38	40.06 ± 0.24	49.53 ± 1.01	0.34 ± 0.05	10.29 ± 1.25	0.17 ± 0.03	0.17 ± 0.01	59 ± 9	58 ± 12	130 ± 25	137 ± 82	39		
CF	60	208	88.81 ± 0.58	40.08 ± 0.26	47.49 ± 0.43	0.27 ± 0.01	10.67 ± 0.54	0.18 ± 0.02	0.22 ± 0.01	60 ± 10	77 ± 46	165 ± 94	137 ± 32	30	194	205
CF	169	84	89.04 ± 0.45	39.57 ± 0.17	47.80 ± 0.28	0.31 ± 0.03	10.49 ± 0.44	0.18 ± 0.02	0.21 ± 0.01	60 ± 11	84 ± 43	138 ± 34	138 ± 64	8	79	
Melf-7	70	112	86.50 ± 1.59	40.04 ± 0.46	47.24 ± 1.52	0.37 ± 0.03	13.12 ± 1.34	0.25 ± 0.06	0.08 ± 0.01	72 ± 20	84 ± 21	<dl	98 ± 78	83		111
Melf-7	128	89	82.36 ± 0.52	39.05 ± 0.39	43.89 ± 0.58	0.36 ± 0.01	16.76 ± 0.40	0.43 ± 0.04	0.05 ± 0.00	79 ± 18	122 ± 17	<dl	128 ± 29	87		
Melf-7	153	95	86.35 ± 1.03	39.77 ± 0.20	46.66 ± 0.77	0.35 ± 0.03	13.14 ± 0.93	0.25 ± 0.04	0.08 ± 0.01	74 ± 21	81 ± 47	<dl	79 ± 44	60		94
Melf-7	180	139	86.91 ± 1.07	39.71 ± 0.28	47.43 ± 0.89	0.34 ± 0.01	12.73 ± 0.96	0.24 ± 0.04	0.09 ± 0.01	71 ± 21	75 ± 23	59	82 ± 33	77	1	137
Melf-7	57	117	88.02 ± 1.20	40.18 ± 0.25	48.26 ± 1.03	0.35 ± 0.03	11.70 ± 1.06	0.20 ± 0.05	0.09 ± 0.01	69 ± 15	68 ± 22	64 ± 4	90 ± 45	88	12	106
SV	47	68	91.20 ± 2.24	40.65 ± 0.66	50.52 ± 1.93	0.42 ± 0.30	8.66 ± 1.95	0.13 ± 0.07	0.16 ± 0.04	81 ± 40	102 ± 22	362 ± 77	43 ± 17	17	66	42
SV	51	34	89.11 ± 5.24	39.77 ± 0.92	48.65 ± 4.27	0.56 ± 0.57	10.43 ± 4.62	0.19 ± 0.16	0.30 ± 0.15	195 ± 100	100 ± 31	362 ± 153	60 ± 39	13	31	23
SV	52	45	87.12 ± 4.42	39.44 ± 0.78	47.01 ± 3.67	0.86 ± 0.58	12.26 ± 3.87	0.24 ± 0.14	0.12 ± 0.05	127 ± 42	95 ± 26	279 ± 119	63 ± 26	25	32	39
SV	98	41	90.14 ± 2.91	40.31 ± 0.43	49.26 ± 2.19	0.14 ± 0.01	9.56 ± 2.67	0.11 ± 0.03	0.49 ± 0.10	77 ± 34	83 ± 28	505 ± 75	112 ± 36	31		
SV	127	67	91.43 ± 1.14	41.04 ± 0.46	50.72 ± 1.18	0.40 ± 0.34	8.47 ± 1.00	0.11 ± 0.04	0.18 ± 0.05	84 ± 41	100 ± 15	369 ± 104	38 ± 13	5		50
SV	OlPla	47	94.89 ± 3.34	41.30 ± 0.73	54.05 ± 3.19	0.27 ± 0.43	5.11 ± 3.13	0.08 ± 0.07	0.07 ± 0.03	92 ± 46	67 ± 34	163 ± 87	83 ± 32	13	12	44

[a] N = total number of points analyzed in each olivine.
[b] Fo (mol.%) = [Mg/(Mg + Fe)].
[c] All iron expressed as FeO.
[d] nTi = Number of points analyzed with Ti concentrations above detection limit.
[e] nCr = Number of points analyzed with Cr concentrations above detection limit.
[f] nP = Number of points analyzed with P concentrations above detection limit.
[g] < dl = concentration lower than detection limit.

the samples, as were the concentrations in individual olivine crystals. The relative standard deviation calculated from the span of P concentrations within each sample ranged from 22 to 91 % for olivines based on the LA-ICP-MS measurements (Supplementary Table 2) and from 22 to 69% for MI (Table 4). Inter and intra-crystal variability in P concentrations of olivines for each sample shown by EPMA transects was also high with 15–79% relative standard deviation (Figs. 2, 3 and Table 3). The olivines showed larger variations in P concentrations than their MI in all samples, except in those of the San Venanzo KAM and Campi Flegrei SHO. No clear correlations were observed between the P and Fo contents of olivines (Fig. 4), nor between the P concentrations of the olivines immediately adjacent to MIs and their respective MI (Fig. 5a). In addition, no obvious relationship between P concentration of the olivines and that of their host lavas (Table 1) was found (Fig. 5b).

Olivines from Ernici-Roccamonfina (HKS, CA, HKCA, SHO series), Roman (SHO series and HKS except Sabatini) and San Venanzo (KAM) are all marked by low P concentrations ($\leq$107 ppm, Fig. 4) based on both LA-ICP-MS and EPMA datasets, and EPMA transects in olivines show relatively weak zoning in P (e.g., Fig. 9) with the exception of a SHO sample from Latera (Lat-23) that shows clear zoning with higher P concentrations ($\leq$160 ppm P) and a single phenocryst with up to 260 ppm P in a HKS sample from Colli Albani (Alb-1 36). Olivines from Campanian, Roman (Sabatini HKS), and Vulture samples displayed elevated P concentrations (up to 435 ppm) with large inter- and intra-crystal variations in each sample (Figs. 2, 3 and Tables 3, 4).

Zoning in P was observed in almost all olivines included in this study. Elemental mapping revealed frequent oscillatory zoning in P (Figs. 2a–c and 3b) either as very fine ($\sim$2 μm, e.g., Fig. 2b and c) or rather wide ($\sim$100 μm, e.g., Fig. 3b) concentric bands. Fine feathery P-rich bands and very distinct patchy zoning was observed in olivine Sab5-14 (Fig. 3a), which displayed an almost homogenous distribution of Al and Cr.

Sector zoning is present in combination with oscillatory zoning (Figs. 2c and 3b). Phosphorous-rich zones are sometimes terminated or cut by P-poor domains (e.g., Figs. 2b and 3b) and melt inclusions/embayments were almost always found in direct contact with P-poor domains even if they cross cut P-rich zones (e.g., profile 2 in Fig. 2a and profile 6 in Fig. 3b). Even though EPMA transects revealed zoning in Al and Cr in some olivines, WDS mapping was unable to distinguish more than the most prominent features due to minor differences between the background and sample signals. Therefore EPMA transects provided better constraints on zoning in Al and Cr.

It is important to note that the LA-ICP-MS dataset (Supplementary Table 2) provides spatially-integrated average concentrations, whereby multiple bands with varying P concentrations can be incorporated in a single spot analysis at the scale of the ablated volume obtained with an 80 μm diameter laser beam. The variations in P concentrations are often present on a much finer scale of a few to several tens of micrometres based on the microprobe mapping

Table 4
Linear regression results for coupled substitutions in olivine phenocrysts.

Sample	Grain ID	Linear Regression Results
P-Al		
Colli Albani HKS		$P = 1.5848 \times Al - 2 \times 10^{-3}, r^2 = 0.997$
Roccamonfina HKCA		$P = 0.557 \times Al - 5 \times 10^{-5}, r^2 = 0.893$
Campi Flegrei SHO		$P = 0.929 \times Al + 2 \times 10^{-4}, r^2 = 0.450$
Alb-1	36 (P-rich)	$P = 1.896 \times Al + 4 \times 10^{-4}, r^2 = 0.472$
Sab-5	22-1 (P-poor)	$P = 0.844 \times Al - 3 \times 10^{-4}, r^2 = 0.723$
Sab-5	22-5 (P-poor)	$P = 0.6214 \times Al + 2 \times 10^{-5}, r^2 = 0.615$
Ves-2	18-3 (spatially correlated P-Al)	$P = 2.6599 \times Al - 3 \times 10^{-4}, r^2 = 0.774$
Ves-2	18-6 (P-poor)	$P = 1.4048 \times Al - 5 \times 10^{-5}, r^2 = 0.591$
P-Cr		
Ernici CA		$P = 1.2221 \times Cr - 3 \times 10^{-4}, r^2 = 0.840$
Campi Flegrei SHO		$P = 1.8339 \times Cr - 3 \times 10^{-4}, r^2 = 0.821$
San Venanzo KAM		$P = 0.1427 \times Cr + 2 \times 10^{-5}, r^2 = 0.570$
Sab-5	14-5 (spatially correlated P-Cr)	$P = 1.5872 \times Cr - 4 \times 10^{-4}, r^2 = 0.855$
Cr-Al		
Campi Flegrei SHO		$Cr = 0.5839 \times Al + 3 \times 10^{-4}, r^2 = 0.728$
Latera SHO		$Cr = 0.5459 \times Al + 2 \times 10^{-4}, r^2 = 0.665$
Lat-23	158-1 (P-poor)	$Cr = 0.5778 \times Al + 9 \times 10^{-5}, r^2 = 0.674$
Lat-23	158-2 (P-poor)	$Cr = 0.7288 \times Al - 8 \times 10^{-5}, r^2 = 0.552$
Al-Ti		
Campi Flegrei SHO		$Al = 4.3737 \times Ti + 8 \times 10^{-5}, r^2 = 0.708$
Vulture HKS		$Al = 2.6931 \times Ti + 6 \times 10^{-5}, r^2 = 0.517$
Melf-7	70	$Al = 1.0047 \times Ti + 3 \times 10^{-4}, r^2 = 0.253$
Melf-7	153	$Al = 1.194 \times Ti + 2 \times 10^{-4}, r^2 = 0.314$
Melf-7	180-4 (sector zoning in P)	$Al = 1.6983 \times Ti + 5 \times 10^{-5}, r^2 = 0.820$

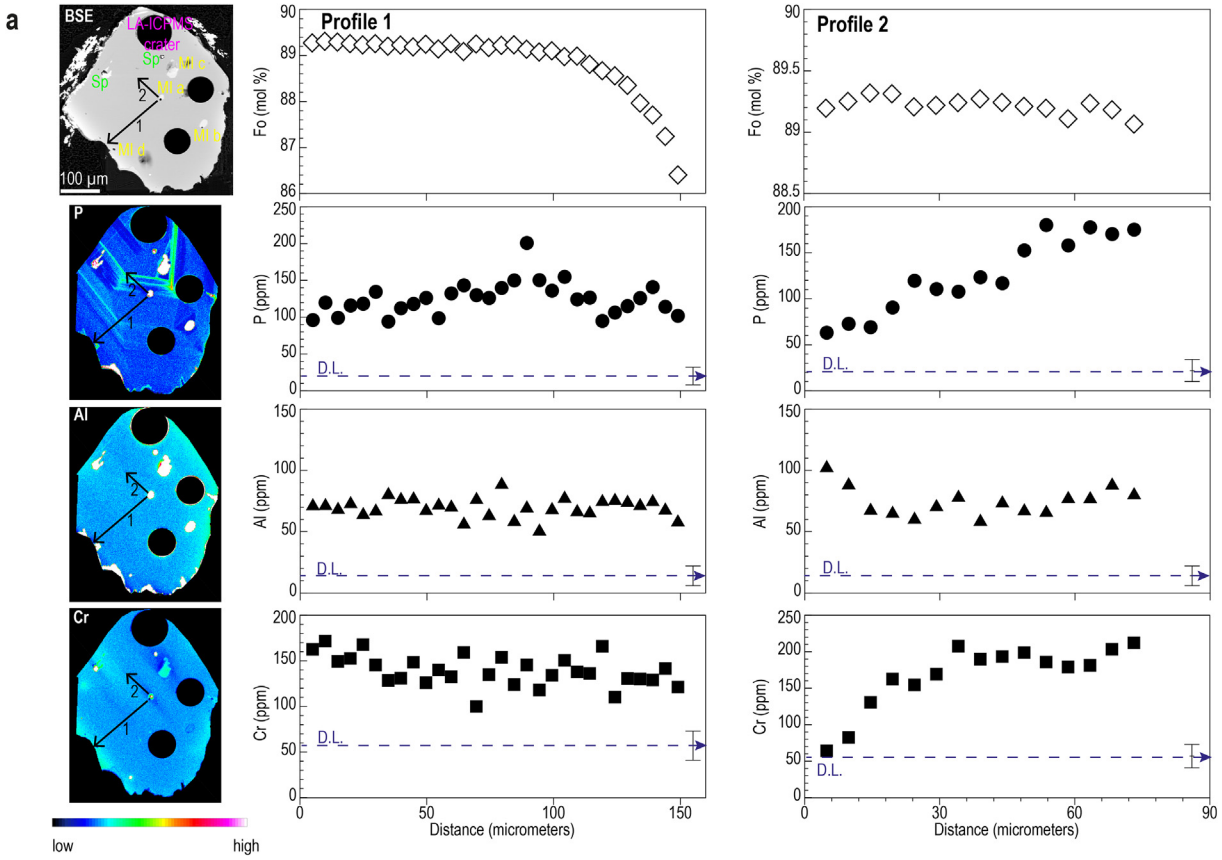

Fig. 2. Electron microprobe X-ray maps and traverses in olivine phenocrysts. (a) Core-to-rim (profile 1) and around-melt-inclusion (profile 2) traverses in olivine CF 169. (b) Melt inclusion-to-rim (profile 3) traverse in olivine Melf-7 70. Note that Cr concentrations in this profile were below detection limit and are not reported. (c) Core-to-rim (profile 4) traverse starting around 35 µm away from melt inclusion in olivine Sab-5 22. Traverse locations are shown in the backscatter electron (BSE) images. Error bars shown in the lower right corner of each diagram are two standard deviations based on counting statistics. Centre of the error bar corresponds to the detection limit for each element. Laser ablation craters (80 µm in diameter) can be seen in each figure. Wherever present, adhering melt is labelled as "gl" in the backscatter image. Data for each profile is reported in Supplementary Table 3. Note that Fo variations in profiles 1 and 3 have no equivalent in P contents, and that P and Fo zoning is decoupled. Profile 4 shows strong P zoning with fine-scale oscillatory and sector zoning patterns, the latter corresponding to the stepwise increase in P in the second half of the transect, at relatively constant Fo contents.

and transect data (Figs. 2 and 3). We thus consider the LA-ICP-MS dataset representative of averaged P concentrations in each olivine, which can be used for characterization of olivine populations in a given volcanic province or magma series. We also adopted this approach to benefit from the much better time effectiveness of data collection via LA-ICP-MS analysis relative to EPMA spot analysis.

4.2. Trace element concentrations in olivines

To investigate the substitution mechanisms of P during crystallization of the Italian olivines, Al, Cr, Ti, Na, Li concentrations were determined by LA-ICP-MS, and zoning in Al, Cr, and Ti was further investigated by EPMA Kα X-ray elemental maps and transects.

Based on the LA-ICP-MS dataset, most of the olivines are characterized by low (≤200 ppm) and fairly homogeneous Al contents within each sample, with the exception of four olivines in SHO samples from Latera, where concentrations range between 100 and 455 ppm (Fig. 6a, Supplementary Table 2). Titanium concentrations in the Italian olivines are very low (≤70 ppm), fairly homogeneous, and show a negative correlation with forsterite content (Fig. 6b). Chromium contents determined by LA-ICP-MS are generally low as well (≤450 ppm), although olivines in the KAM sample from San Venanzo contain up to 600 ppm Cr (Fig. 6c). Even the highest Cr concentrations documented here are much lower than values reported for olivines from ugandites (506–619 ppm, Foley et al. (2011)) or ocean island basalts (616–896 ppm, Nikogosian and Sobolev (1997); up to 1423 ppm Sobolev et al. (2007)). Chromium concentrations are strongly correlated with forsterite content (Fig. 6c), consistent with behaviour observed in ocean island basalts (Sobolev et al., 2007).

Within all of the analysed samples, only olivines from Vulsini HKS, Roccamonfina HKS, and San Venanzo KAM were found to contain detectable amounts of Li (Supplementary Table 2). In the olivines from these samples, Li concentrations are extremely high, up to 77 ppm, in comparison with the data published for magmatic

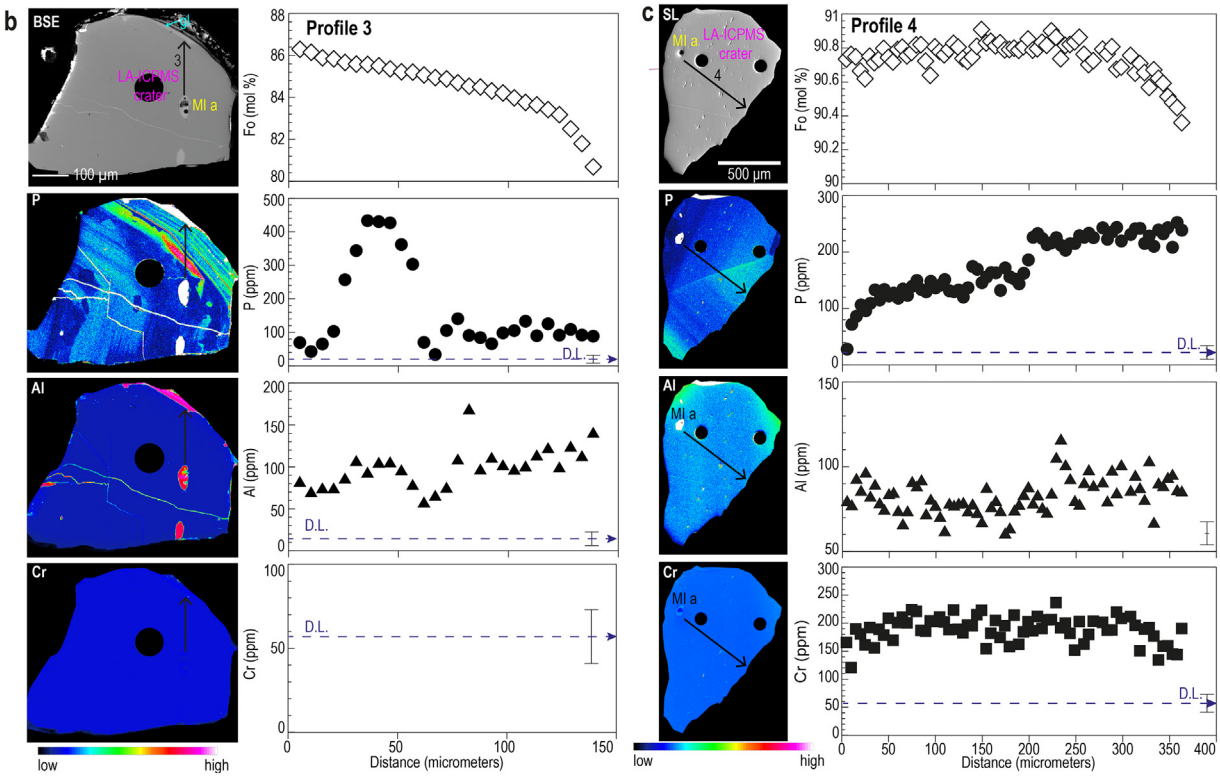

Fig 2. *(continued)*

(0.87–3.52 ppm, Nikogosian and Sobolev, 1997; De Hoog et al., 2010; Foley et al., 2011) and mantle (0.32–2.38 ppm, Mallmann et al., 2009; De Hoog et al., 2010) olivines. Sodium was only detectible in olivines from Vulsini HKS, Latera HKS and SHO, and Vulture HKS samples with concentrations <50 ppm, which is lower than that reported for olivines from ugandites (108–266 ppm, Foley et al., 2011).

4.3. Intracrystal variations in minor and trace elements

The olivine phenocrysts were generally not strongly zoned in divalent cations (Fe, Mg, Ca, Mn, and Ni). Chromium zoning was more prominent and observed more frequently than Al zoning (e.g., Figs. 2a and 3b). Titanium concentrations were very low except in olivines from Vulture, and no significant zoning could be observed outside analytical error. All analysed olivines were zoned in P, generally at a fine scale, with widths of P-rich and P-poor bands varying from a few to several tens of microns, displaying oscillatory, sector and patchy zoning patterns (see P Kα X-ray maps in Figs. 2 and 3). Interiors of olivine phenocrysts from the San Venanzo KAM sample, characterized by high-Fo contents ($Fo_{91.3}$-$Fo_{93.1}$), were not zoned in any cations and had very low P concentrations (mostly $\leq$ 22 ppm, but occasionally reaching up to 63 ppm (Fig. 9). Phosphorous zoning was in most cases not correlated with zoning in any other element or in Fo content. Late-stage crystallization of the phenocryst rims or re-equilibration at the rims with evolved melts had apparently no effect on P, and significant variation in P content was observed in otherwise uniform Fo-rich phenocryst cores (cf. Fig. 2), suggesting that P zoning is generally independent from crystal fractionation. Positively correlated P-Al-Cr zoning as observed by Milman-Barris et al. (2008) was not found in the Italian olivines, except for a few cases of spatial correlations between P and Al, where EPMA transects in three olivine grains revealed similar profiles in and a positive correlation between in P and Al (Fig. 7a).

In all analysed olivine phenocrysts, irrespective of the P concentrations or strong zoning in the interiors, MIs were generally surrounded by P-poor domains (profiles 2, 3 in Fig. 2 and profile 6 in Fig. 3). The P-poor domains are usually enriched in Al (and Ti if detected), and depleted in Cr (e.g., Fig. 2a profile 2 and Fig. 3b profile 6). Wherever present, Al-enriched and Cr-depleted zones surrounding MIs were larger than the corresponding low-P zones around MIs.

5. DISCUSSION

5.1. Relationship between P and possible charge-balancing cations

Incorporation of P^{5+} into the olivine structure replacing Si^{4+} in the tetrahedral site (Boesenberg et al., 2004; Boesenberg and Hewins, 2010) requires a charge balancing mechanism involving either vacancies or coupled substitutions with trivalent or monovalent cations. Focusing on mechanisms involving trivalent cations, charge balance

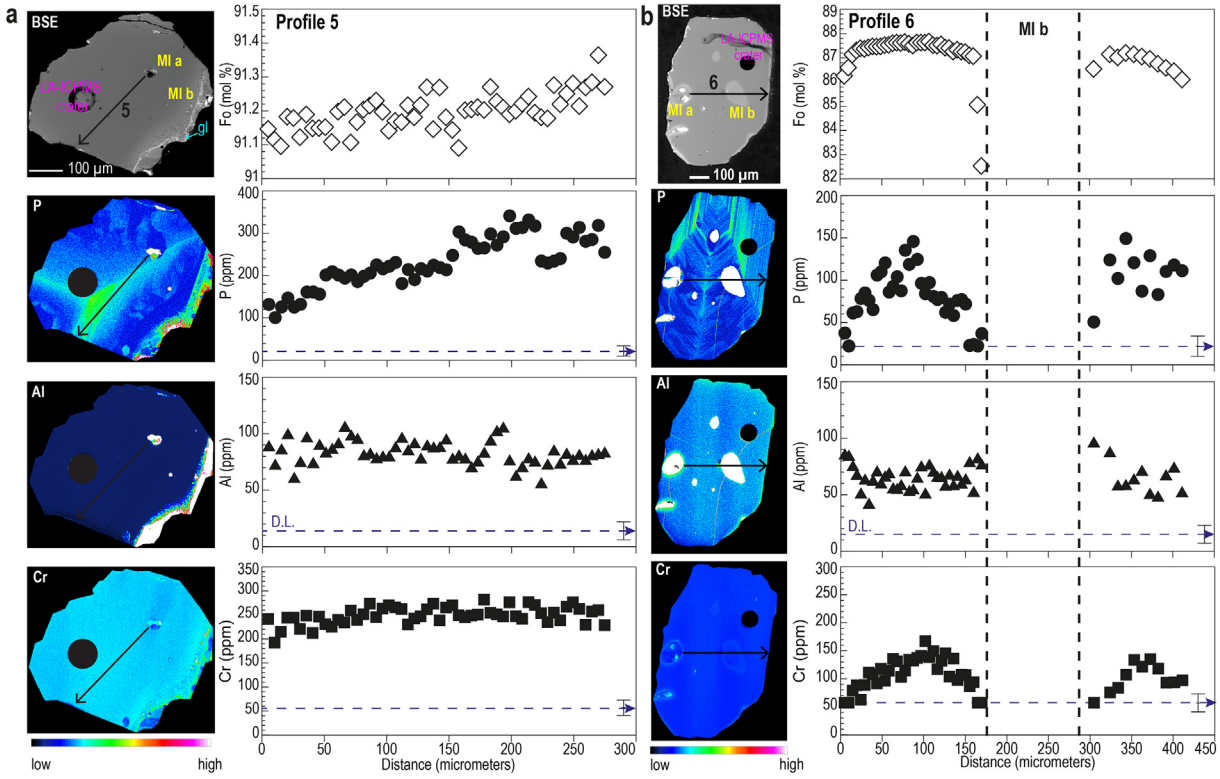

Fig. 3. Electron microprobe X-ray maps and traverses in olivine phenocrysts. (a) Core-to-rim (profile 5) traverse starting around 25 µm away from melt inclusion in olivine Sab-5 14. (b) Melt inclusion-to-rim (profile 6) traverse starting in olivine immediately adjacent to MI a and progressing towards the rim through MI b in olivine Ves-2 130. Boundaries of MI b are indicated with vertical dashed lines. Traverse locations are shown in the backscatter electron (BSE) images. Error bars shown in the lower right corner of each diagram are two standard deviations based on counting statistics. Centre of the error bar corresponds to the detection limit for each element. Laser ablation craters (80 µm in diameter) are visible in each figure. Wherever present, adhering melt is labelled as "gl" in the backscatter image. Data for each profile is reported in Supplementary Table 3.

can be maintained by (1) substitution of trivalent ions as Al^{3+} and Cr^{3+} replacing Mg^{2+} on an M site (Milman-Barris et al., 2008); (2) substitution of trivalent ions as Al^{3+} and Cr^{3+} replacing Mg^{2+} on an M site (Mallmann et al., 2009) with (a) equal Al^{3+} and Cr^{3+} M-site occupancy, or (b) total M-site occupancy either by Al^{3+} or Cr^{3+}); (3) substitution of trivalent ions such as Al^{3+} and Cr^{3+} replacing Si^{4+} on a T site (Grant and Kohn, 2013), according to the following reactions:

$$^{iv}Si^{4+} + 5^{vi}M^{2+} = {}^{iv}P^{5+} + {}^{vi}Cr^{3+} + 2^{vi}Al^{3+} + 2^{vi}[] \quad (1)$$

$$^{iv}Si^{4+} + 2^{vi}M^{2+} = {}^{iv}P^{5+} + {}^{vi}(Al,Cr)^{3+} + {}^{vi}[] \quad (2)$$

$$^{iv}Si^{4+} = 0.5^{iv}P^{5+} + 0.5^{iv}(Al,Cr)^{3+} \quad (3)$$

However, both Al^{3+} and Cr^{3+} have charge balancing mechanisms not involving P that might interfere with a straightforward interpretation of presence or absence of correlations between P, Al, and Cr. Some of these possible mechanisms include (4) charge coupled substitution of Al^{3+} together with Cr^{3+} where one M site is occupied by (Al^{3+} and/or Cr^{3+}) and a T site by Al^{3+} (De Hoog et al., 2010) with (a) full Cr^{3+} M-site occupancy, or (b) equal Al^{3+} and Cr^{3+} M-site occupancy; (5) charge coupled substitution of trivalent ions as Al^{3+} and Cr^{3+} replacing Mg^{2+} on an M site, and Al^{3+} replacing Si^{4+} on a T site (Milman-Barris et al., 2008); (6) Tschermak's type $MgCr^{3+}Al^{3+}O_4$ substitution (Jollands et al., 2018); (7) Coupled Ti^{3+}/Ti^{4+} and Al^{3+} substitution (Jollands et al., 2016) as (a) $(MgTi^{3+})AlO_4$, or (b) $(Mg_{3/2}Ti^{4+}_{1/2})AlO_4$, as represented by reactions

$$^{iv}Si^{4+} + {}^{vi}M^{2+} = {}^{iv}Al^{3+} + {}^{vi}(Al,Cr)^{3+} \quad (4)$$

$$^{iv}Si^{4+} + 2.5^{vi}M^{2+} = {}^{iv}Al^{3+} + {}^{vi}Cr^{3+} + {}^{vi}Al^{3+} + 0.5^{vi}[] \quad (5)$$

$$^{iv}Si^{4+} + {}^{vi}M^{2+} = {}^{iv}Al^{3+} + {}^{vi}Cr^{3+} \quad (6)$$

$$^{iv}Si^{4+} + {}^{vi}M^{2+} = {}^{iv}Al^{3+} + {}^{vi}Ti^{3+} \quad (7a)$$

$$^{iv}Si^{4+} + {}^{vi}M^{2+} = {}^{iv}Al^{3+} + 1.5^{vi}Mg^{2+} + 0.5^{vi}Ti^{4+} \quad (7b)$$

Although there is no overall correspondence of zoning patterns for P, Al and Cr in Italian olivines, concentrations of these cations correlate positively in some samples (Fig. 7a and b). Roughly linear trends in plots of P versus Al (Fig. 7a) and P versus Cr (Fig. 7b) and variability in the slopes of linear regression lines (Table 4) suggest that multiple substitution mechanisms control the incorporation of these cations into the olivine structure. Most of the data in P-Al space (Fig. 7a) fall between the lines plotted for reactions (1), (2), and (3), indicating that some combination of these reactions provided the charge balance for P^{5+} incorporations. It is important to note that not all P is charge-balanced by a combination of substitution

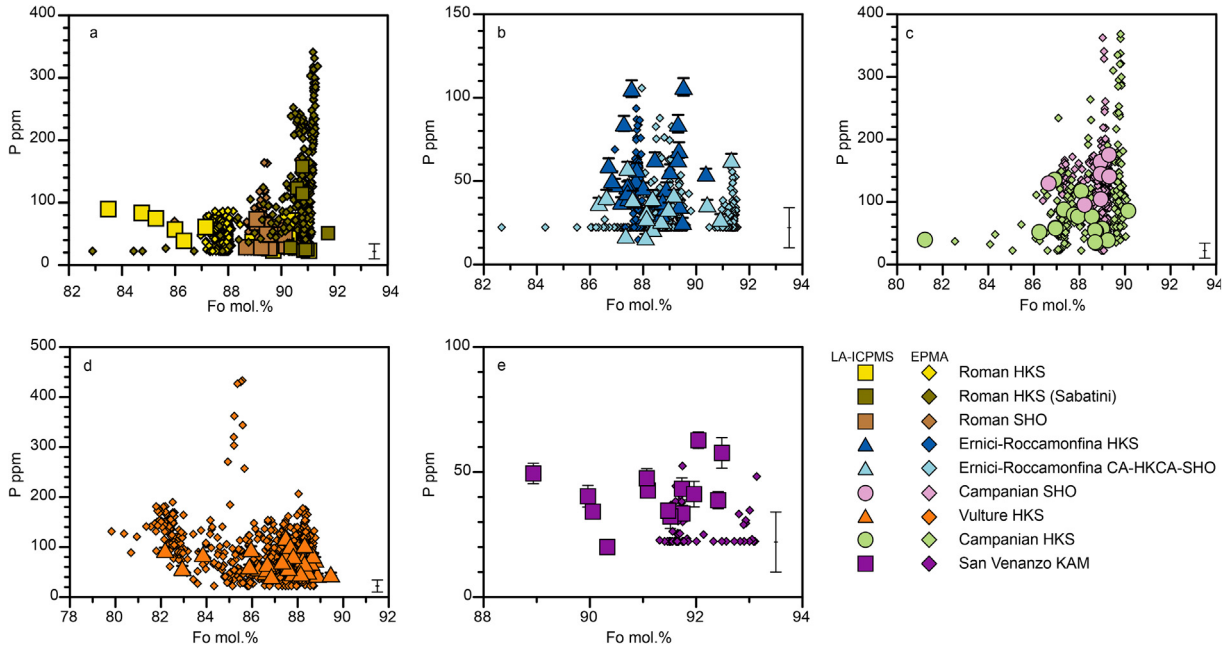

Fig. 4. Forsterite, determined by EPMA, versus P contents of olivines (EPMA transects represented by small diamonds and LA-ICP-MS spot analysis by large symbols for each sample). LA-ICP-MS error bars, where larger than the symbol size, represent one standard deviation based on counting statistics. EPMA error bars, shown in the lower right corner of each diagram, are two standard deviations based on counting statistics. Data for each volcanic centre are presented separately, and are reported in Supplementary Tables 2 and 3. (a) Roman Province, (b) Ernici-Roccamonfina, (c) Campania, (d) Vulture, (e) Intra-Apennine Province.

mechanisms considered here, as positive intercepts for P in P-Al space for Campi Flegrei SHO olivines, and Alb1-36, Sab5-22 transects indicate (Table 4). In P-Cr space, however, other mechanisms not considered here probably play a role in charge balancing the P^{5+} substitution, as only the data from Campanian SHO olivine point to a combination of reaction (1) and (2). Aluminium and Cr concentrations are positively correlated in Campanian SHO and Latera SHO samples (Fig. 7c), with slopes of 0.58 and 0.55 in atomic proportions, respectively, in agreement with trends in Hawaiian olivines that experienced short high-temperature histories (Milman-Barris et al., 2008). Charge balance is possibly achieved by a combination of mechanisms represented by reactions (1)–(6) since most data plot between the lines representing these reactions. Nonetheless, positive intercepts for Cr in Al-Cr space (Fig. 7c) indicate that the incorporation of this element in the olivine is not entirely charge-balanced by coupled substitutions with Al. Titanium and Al concentrations in Italian olivines show positive correlations (Fig. 7d), which was also observed in Ugandan (Foley et al., 2011) and Hawaiian (Milman-Barris et al., 2008) olivines. The Ti-Al pair again defines roughly linear trends with highly variable slopes (0.54–4.4 in atomic proportions) pointing to multiple substitution mechanisms, since Ti and Al can reside both in the tetrahedral and in the octahedral sites, and several substitution mechanisms may operate. This variability of trends in pairs of P, Al, Cr or Ti suggests the likelihood that a combination of substitution mechanisms is involved in incorporation of these elements into the olivine structure (Milman-Barris et al., 2008).

5.2. Phosphorous in olivines and melt inclusions from different rock series

The phosphorous contents of olivine-hosted MIs from central-Italian rocks have been previously found to increase with increasing K content (Kamenetsky et al., 1995; Nikogosian and van Bergen, 2010; Nikogosian et al., 2016). This is confirmed by this study, where MIs from HKS samples have slightly higher P contents than those from SHO, CA, or HKCA samples (Fig. 5c). Primitive MIs and their olivine hosts from Roccamonfina and Ernici show similar systematics, as their P contents increase from CA to HKS samples (Ernici), and from SHO to HKCA to HKS samples (Roccamonfina), suggesting P_2O_5 content of the melt as a possible control on P uptake by olivines. However, this relationship is reversed at Latera, where olivines from the SHO sample contain more P than those from the HKS sample, despite the higher P content in the melt of the latter (Fig. 5d).

Melts with similar P contents crystallized olivines with significantly different P contents. For example, the maximum P contents of olivines in HKS melts with up to 1.40 wt.% P_2O_5 are 370 ppm at Sabatini, and only 90 ppm at Vulsini (Fig. 5d). On the other hand, Campi Flegrei SHO and Somma-Vesuvius HKS melts with up to 1.61 wt.% and 1.89 wt.% P_2O_5 both crystallized olivines with maximum P contents of 362 and 368 ppm, respectively. Hence, relationships between the P contents of the melt and coexisting olivines are not straightforward, and differences between the magma series not systematic. This suggests that the P concentrations in olivines do not only

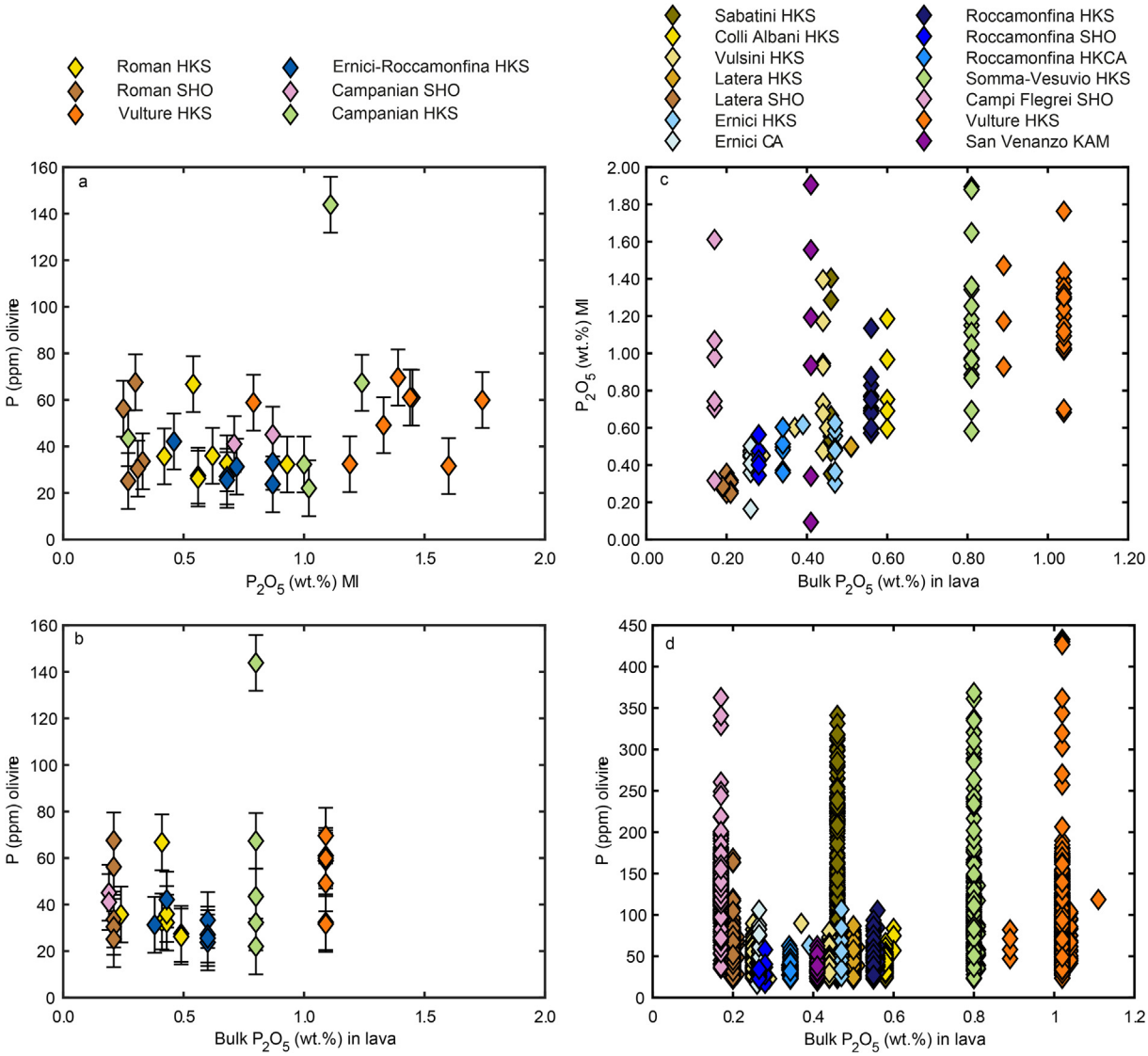

Fig. 5. Variation of P content in (a) olivines immediately adjacent to melt inclusions (based on EPMA traverses) and in melt inclusions (EPMA) and (b) olivines immediately adjacent to melt inclusions (based on EPMA traverses) and bulk rock samples (XRF). Error bars, where larger than the symbol size, are two standard deviation based on counting statistics. Reported P concentrations are for olivine directly adjacent to the boundary with a melt inclusion (given in Table 5). Deviations from olivine stoichiometry in spot analyses were used to determine exact locations of olivine–MI boundaries. (c) P_2O_5 concentrations of all the melt inclusions (EPMA) analysed versus P_2O_5 concentrations of bulk rock samples (XRF), (d) P concentrations of all analysed olivines (both LA-ICP-MS and EPMA data, same range as in Fig. 2) versus P_2O_5 concentrations of bulk rock samples (XRF).

depend on the melt composition (P and K contents specifically) but that other factors are involved as well. They will be explored in the following sections.

5.3. Factors controlling the P concentrations in olivines

5.3.1. Effect of melt composition

Published equilibrium olivine-silicate melt distribution coefficients for P determined in terrestrial samples cover a range on the order of 0.01–0.28 (Anderson and Greenland, 1969; Brunet and Chazot, 2001; Foley et al., 2011; Baziotis et al., 2017). Given the compositional diversity of Italian potassic melts and the wide variation of their P contents, pairs of olivines and their MIs should provide insight in the extent to which the melt composition controls the P partitioning. However, as discussed below, zoning in olivines may obscure a clear relationship.

As demonstrated here and in previous studies (Spandler et al., 2007; Milman-Barris et al., 2008; Hofmann, 2010; Foley et al., 2011; Welsch et al., 2013, 2014; Shea et al., 2015), magmatic olivines generally exhibit fine-scale oscillatory, patchy or sector zoning for P, so that concentrations may vary significantly in adjacent portions of a crystal. Identifying concentration values that should represent equilibrium with coexisting melt is therefore not straightforward. Baziotis et al. (2017) have recently discussed the

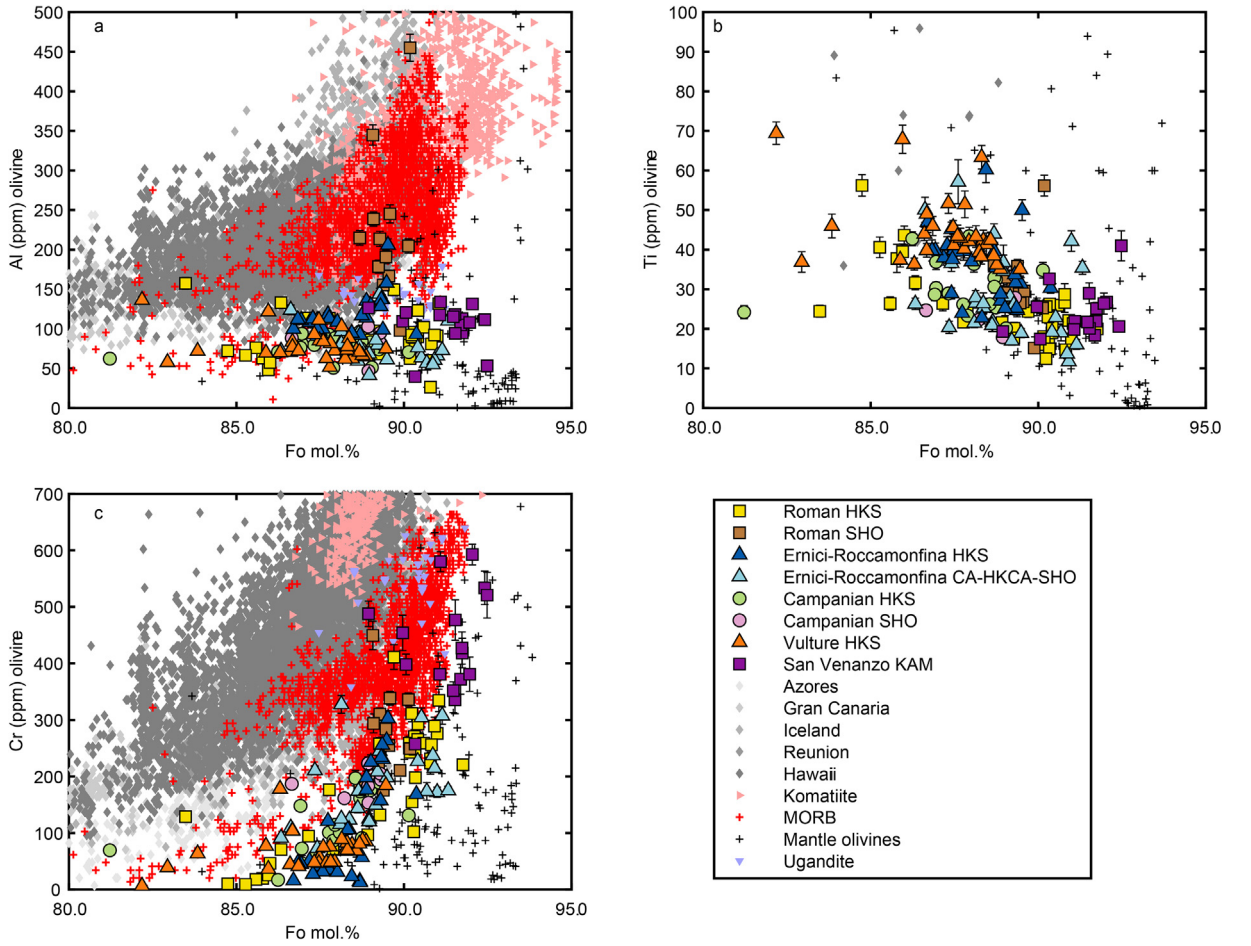

Fig. 6. Forsterite (EPMA) versus (a) Al, (b) Ti and (c) Cr contents in olivines (LA-ICP-MS). Error bars, where larger than the symbol size are one standard deviation based on counting statistics. Data sources: Azores (Sobolev et al., 2007), Gran Canaria (Sobolev et al., 2007; Gurenko et al., 2010), Iceland (Sobolev et al., 2007), Réunion (Sobolev et al., 2007), Hawaii (Nikogosian and Sobolev, 1997; Sobolev et al., 2007; Milman-Barris et al., 2008), komatiites (Sobolev et al., 2007; Milman-Barris et al., 2008), MORB (Sobolev et al., 2007), mantle olivines (Conticelli and Peccerillo, 1989; Brunet and Chazot, 2001; Mallmann et al., 2009; De Hoog et al., 2010; Sanfilippo et al., 2014), ugandites (Foley et al., 2011).

highly variable P concentrations in secondary olivines from mantle xenoliths and concluded that only the lowest partition coefficients found could be taken as approaching equilibrium values. In an approach to tackle this complication, only composition data from olivines immediately adjacent to an olivine-MI boundary were considered for "apparent" partition coefficient calculations in this study. The location of an olivine–MI boundary was determined based on EPMA spot composition deviations from olivine stoichiometry. Both P Kα X-ray maps and EPMA transects (e.g., Figs. 2 and 3) clearly show that the MIs are surrounded (sometimes partially) by low-P zones. These low-P zones are interpreted as products of near equilibrium crystallization, since the growth rate of the advancing crystal face becomes limited by the diffusion of main olivine constituents (e.g., Si, Fe, Mg) into the boundary layer through a narrow channel connected to the far field melt as the MI is being trapped in the crystallizing olivine, hence eliminating kinetic controls on P uptake such as solute trapping (Reitano et al., 1994).

We calculated a single "apparent" partition coefficient for each MI using the olivine spot composition immediately adjacent to the MI determined by EPMA transects. Results are in the range of 0.0045–0.0524 (Table 5), in line with published values, including those found for other potassic melts (0.01–0.02, Foley et al., 2011).

Olivine crystallization experiments of Grant and Kohn (2013) on Fe-free trachyandesitic compositions demonstrated a clear relationship between the P partition coefficient, the mole fraction of SiO_2 in the melt and the ratio of non-bridging to tetrahedrally coordinated oxygens (NBO/T), indicating increasing partition coefficients with increasing polymerization of the melt. On the other hand, several studies have argued that compositional parameters such as mole fractions should be used instead of "universal melt descriptors" as NBO/T, which may be better suited to exploring physical rather than thermodynamic properties of melts (Evans et al. (2008a)) when investigating melt compositional controls on partitioning behaviour in natural igneous systems (O'Neill and Eggins, 2002; O'Neill and

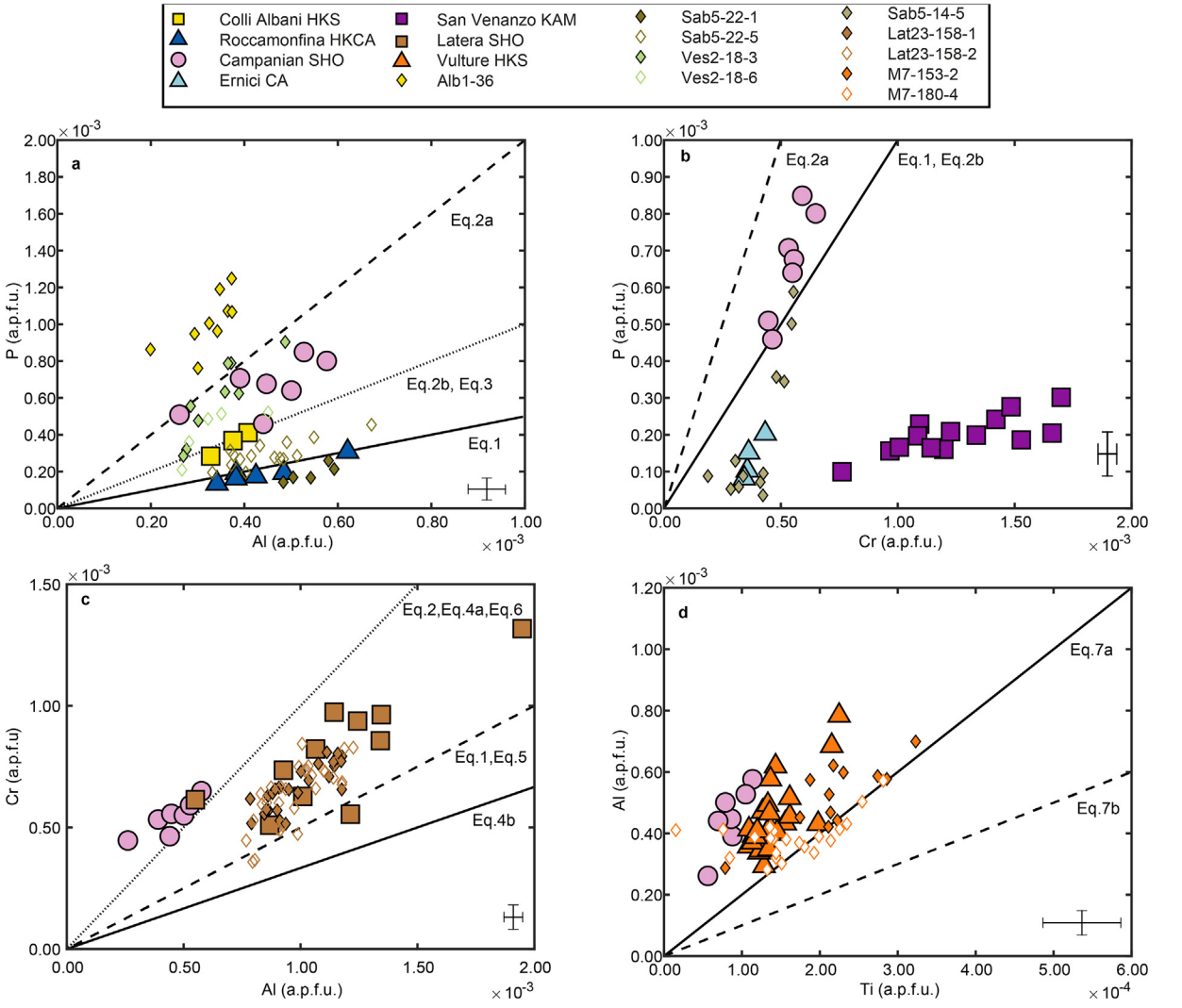

Fig. 7. Relationship among trace elements in olivine, based on LA-ICP-MS analysis (circles) and EPMA transects (diamonds). LA-ICP-MS spot analyses are denoted by circles. Error bars (1 standard deviation) are typically smaller than the symbol size. EPMA transects are shown by diamonds in each diagram; error bars shown in the lower right corner of each diagram represent two standard deviations based on counting statistics. (a) Al versus P, (b) Cr versus P, (c) Al versus Cr, (d) Ti versus Al. See Section 5.1 for reactions that correspond to the lines in each panel. Linear regression results are given in Table 4.

Mavrogenes, 2002; Evans et al., 2008b). Our results support this argument. Taking the mole fraction of a melt component (e.g., X_{SiO2}), calculated on a single cation basis following Evans et al. (2008a), as a proxy to its activity (e.g., a_{SiO2}), the "apparent" partition coefficients for P between olivine and silicate melt show a positive trend with increasing activity of SiO_2 (i.e. increasing polymerization of the melt), and a negative trend with increasing activity of $PO_{2.5}$ and TiO_2 (Fig. 8), whereas no relationship with NBO/T can be discerned. Although the relationships of ln $D_P^{ol/melt}$ with X_{SiO2}, $X_{PO2.5}$, X_{TiO2} are far from linear correlations, they tend to signal a strong compositional control on the partitioning behaviour (cf., Grant and Kohn, 2013). The negative trend with $X_{PO2.5}$ suggests a deviation of P partitioning from Henry's law behaviour, whereas the negative trend with X_{TiO2} might be due to competition between P and Ti for occupancy of the tetrahedral site. Although there is no well-defined trend between ln $D_P^{ol/melt}$ and $X^{NaO0.5}$ or $X_{KO0.5}$, partitioning of P is expected to be affected by the alkali content of mafic magmas since the activity coefficient of P_2O_5 is sensitive to the overall melt composition (Mallmann and O'Neill, 2009) and P_2O_5 can act as a network former or modifier depending on the degree of melt polymerization (Mysen and Richet, 2005 and references therein). More experimental studies are needed to investigate the activity of P, Ti, alkalis and other components as compositional controls on the partitioning behaviour of P.

5.3.2. Melt evolution due to crystal fractionation

Crystal fractionation changes the melt composition and may thus have an effect on the P concentration of crystallizing olivine. During fractionation, D_P is expected to increase, as the melt composition evolves and becomes more polymerized (Grant and Kohn, 2013). As long as apatite remains absent, progressive crystallization of primitive

Table 5
Olivine compositions adjacent to melt inclusions and melt inclusion compositions used in calculation of partition coefficients determined by EPMA. All oxides are reported in wt.%; Ti, Al, Cr, P in olivine reported as ppm.

Olivine compositions

Sample	Olivine Code	SiO_2	MgO	CaO	FeO[a]	MnO	NiO	Total	Ti	Al	Cr	P
Lat-18	42	40.13	47.53	0.62	12.12	0.19	0.13	100.72	77	111	98	27
Lat-18	42	39.79	48.02	0.46	12.29	0.20	0.16	100.93	-[b]	121	65	26
Sab-5	14	40.22	49.64	0.71	9.63	0.17	0.20	100.57	-	123	206	67
Sab-5	22	40.82	49.09	0.73	9.40	0.17	0.13	100.35	77	251	64	33
Vul-14	57	41.06	49.19	0.81	10.46	0.20	0.20	101.93	58	110	111	32
Vul-14	57	40.78	48.91	0.82	10.67	0.20	0.20	101.58	-	114	58	36
Vul-10	55	40.88	49.93	0.51	9.93	0.16	0.17	101.59	66	146	113	36
Lat-22	26	40.27	49.86	0.29	9.96	0.14	0.27	100.79	-	231	188	34
Lat-22	26	39.63	48.71	0.38	11.06	0.16	0.25	100.18	-	197	147	69
Lat-22	26	40.14	50.26	0.28	9.45	0.13	0.28	100.55	-	221	186	30
Lat-23	158	40.65	49.41	0.38	9.38	0.14	0.28	100.23	-	297	215	56
Lat-23	158	41.09	50.48	0.40	9.28	0.13	0.28	101.66	80	309	148	25
Ern-4	362	39.95	46.29	0.55	12.62	0.21	0.14	99.76	101	252	-	42
Ern-5	135	40.86	48.15	0.46	10.94	0.19	0.18	100.79	-	184	181	31
Rocc-7	136	40.37	48.26	0.49	11.99	0.22	0.17	101.50	68	103	-	33
Rocc-7	136	40.59	48.34	0.50	12.06	0.22	0.17	101.87	64	91	-	27
Rocc-7	136	40.64	48.00	0.51	11.93	0.22	0.16	101.45	93	104	-	24
Rocc-7	271	40.42	48.56	0.47	11.19	0.17	0.15	100.96	128	205	-	26
CF	60	39.86	47.65	0.23	10.62	0.17	0.19	98.71	-	152	80	41
CF	169	39.48	47.87	0.24	10.25	0.17	0.19	98.20	81	141	-	45
Ves-2L	130	40.11	44.71	0.60	15.09	0.24	0.14	100.88	79	138	-	32
Ves-2L	130	40.40	47.95	0.39	11.57	0.19	0.18	100.67	-	77	182	22
Ves-2L	130	38.79	39.74	0.36	22.19	0.46	0.12	101.66	-	112	-	43
Ves-2b	18	40.04	49.30	0.49	10.49	0.17	0.14	100.62	-	80	123	144
Ves-2b	18	40.17	49.49	0.42	10.28	0.17	0.15	100.68	-	51	127	67
Melf-7	70	39.84	47.46	0.39	13.44	0.26	0.09	101.48	-	83	-	70
Melf-7	70	40.03	47.40	0.41	13.04	0.24	0.09	101.20	77	111	-	59
Melf-7	180	40.10	48.04	0.39	11.78	0.22	0.09	100.61	136	182	-	61
Melf-7	57	39.04	43.52	0.37	16.58	0.41	0.05	99.97	106	119	-	61
Melf-7	57	40.57	48.81	0.46	11.41	0.17	0.09	101.53	129	125	-	32
Melf-7	57	40.19	47.46	0.36	12.10	0.19	0.09	100.40	72	114	-	32
Melf-7	57	40.37	48.68	0.41	11.03	0.17	0.09	100.76	62	87	-	49
Melf-7	57	40.34	48.31	0.33	11.53	0.18	0.10	100.79	76	103	-	60

Melt inclusion compositions

Sample	MI Code	SiO_2	TiO_2	Al_2O_3	FeO[a]	MnO	MgO	CaO	Na_2O	K_2O	P_2O_5	Total	NBO/T	D_P
Lat-18	42-a	47.05	1.04	17.29	7.19	0.19	6.56	14.17	1.47	4.60	0.56	100.24	0.690	0.0113
Lat-18	42-b	46.57	1.08	17.57	7.19	0.09	6.39	14.13	1.60	4.89	0.56	100.19	0.685	0.0108
Sab-5	14-a	46.40	1.10	13.67	7.22	0.06	8.58	13.93	1.29	7.20	0.54	100.10	0.943	0.0284
Sab-5	22-a	46.13	0.98	14.10	7.21	0.09	8.67	13.19	1.32	7.73	0.68	100.21	0.924	0.0111
Vul-14	57-a	47.51	1.12	18.21	6.01	0.08	6.80	9.17	1.33	8.75	0.93	100.01	0.567	0.0080
Vul-14	57-b	47.88	1.06	17.45	7.21	0.08	8.98	12.54	0.45	3.61	0.62	99.99	0.689	0.0134
Vul-10	55-a	47.32	0.89	16.30	7.21	0.05	9.43	11.98	1.17	5.19	0.42	100.07	0.781	0.0194
Lat-22	26-a	48.80	0.99	16.45	7.22	0.13	8.14	13.02	2.49	2.47	0.33	100.15	0.718	0.0230
Lat-22	26-b	48.47	0.94	16.01	7.22	0.11	8.87	13.43	2.25	2.42	0.30	100.13	0.771	0.0524
Lat-22	26-c	48.66	0.93	16.02	7.19	0.10	9.23	12.75	2.37	2.32	0.31	100.00	0.764	0.0227
Lat-23	158-b	49.35	0.91	16.38	7.24	0.17	8.12	13.25	2.33	2.00	0.25	100.12	0.710	0.0507
Lat-23	158-c	49.22	0.91	16.75	7.21	0.16	8.13	12.81	2.37	2.15	0.27	100.10	0.691	0.0213
Ern-4	362-a	48.13	0.74	16.77	7.50	0.11	8.84	11.72	0.60	5.02	0.46	100.04	0.702	0.0212
Ern-5	135-a	46.91	1.26	15.67	8.50	0.12	9.50	16.10	0.35	0.74	0.72	100.00	0.850	0.0099
Rocc-7	136-a	45.24	1.38	16.97	8.00	0.14	7.67	15.59	1.25	3.17	0.87	100.39	0.799	0.0088
Rocc-7	136-b	42.54	1.28	16.76	7.51	0.12	5.79	14.50	2.24	8.71	0.68	100.27	0.832	0.0091
Rocc-7	136-c	46.80	1.36	16.94	8.00	0.07	8.10	15.77	0.54	1.81	0.87	100.37	0.760	0.0062
Rocc-7	271-a	44.60	1.71	16.88	7.54	0.09	7.13	15.33	1.28	4.95	0.68	100.33	0.785	0.0087
CF	60-a	47.47	0.97	13.31	7.11	0.13	7.96	15.07	2.29	4.88	0.71	100.01	0.931	0.0133
CF	169-a	48.23	0.90	15.51	7.13	0.04	7.72	11.36	2.39	6.09	0.87	100.35	0.746	0.0118
Ves-2L	130-a	46.07	1.16	18.67	7.14	0.08	5.68	10.68	2.29	7.55	1.00	100.45	0.585	0.0074
Ves-2L	130-b	46.28	1.10	15.65	7.13	0.13	7.35	13.50	2.13	6.08	1.02	100.51	0.799	0.0049

(*continued on next page*)

Table 1 (*continued*)

Melt inclusion compositions														
Sample	MI Code	SiO_2	TiO_2	Al_2O_3	FeO[a]	MnO	MgO	CaO	Na_2O	K_2O	P_2O_5	Total	NBO/T	D_P
Ves-2L	130-c	49.23	0.53	22.70	6.95	0.17	2.83	7.95	3.59	5.68	0.27	100.00	0.284	0.0372
Ves-2b	18-a	45.91	1.38	14.53	7.09	0.04	7.25	14.11	2.06	6.41	1.11	100.02	0.854	0.0296
Ves-2b	18-b	46.62	1.34	14.74	7.07	0.06	7.18	13.16	2.01	6.85	1.24	100.41	0.811	0.0125
Melf-7	70-a	45.74	2.04	16.73	7.49	0.16	6.34	14.24	1.49	4.22	1.39	100.00	0.685	0.0115
Melf-7	70-b	48.46	2.02	18.13	7.49	0.22	6.59	11.36	2.52	2.27	0.79	100.00	0.544	0.0172
Melf-7	180-a	44.34	2.34	13.95	7.49	0.37	6.67	20.97	1.45	0.81	1.45	100.00	0.957	0.0096
Melf-7	57-a	46.19	1.55	18.32	7.49	0.33	5.49	12.47	4.00	2.56	1.44	100.00	0.594	0.0097
Melf-7	57-b	40.62	1.99	15.94	7.49	0.06	5.98	19.12	2.56	4.90	1.19	100.00	0.959	0.0063
Melf-7	57-c	40.32	2.53	17.32	7.49	0.13	6.43	19.78	1.50	2.73	1.60	100.00	0.877	0.0045
Melf-7	57-e	43.99	2.17	17.21	7.48	0.11	6.49	12.58	3.49	5.00	1.33	100.00	0.713	0.0084
Melf-7	57-f	43.77	2.53	16.49	7.46	0.10	6.38	12.63	3.39	5.36	1.74	100.00	0.733	0.0079

[a] All iron expressed as FeO.
[b] Concentration lower than detection limit.

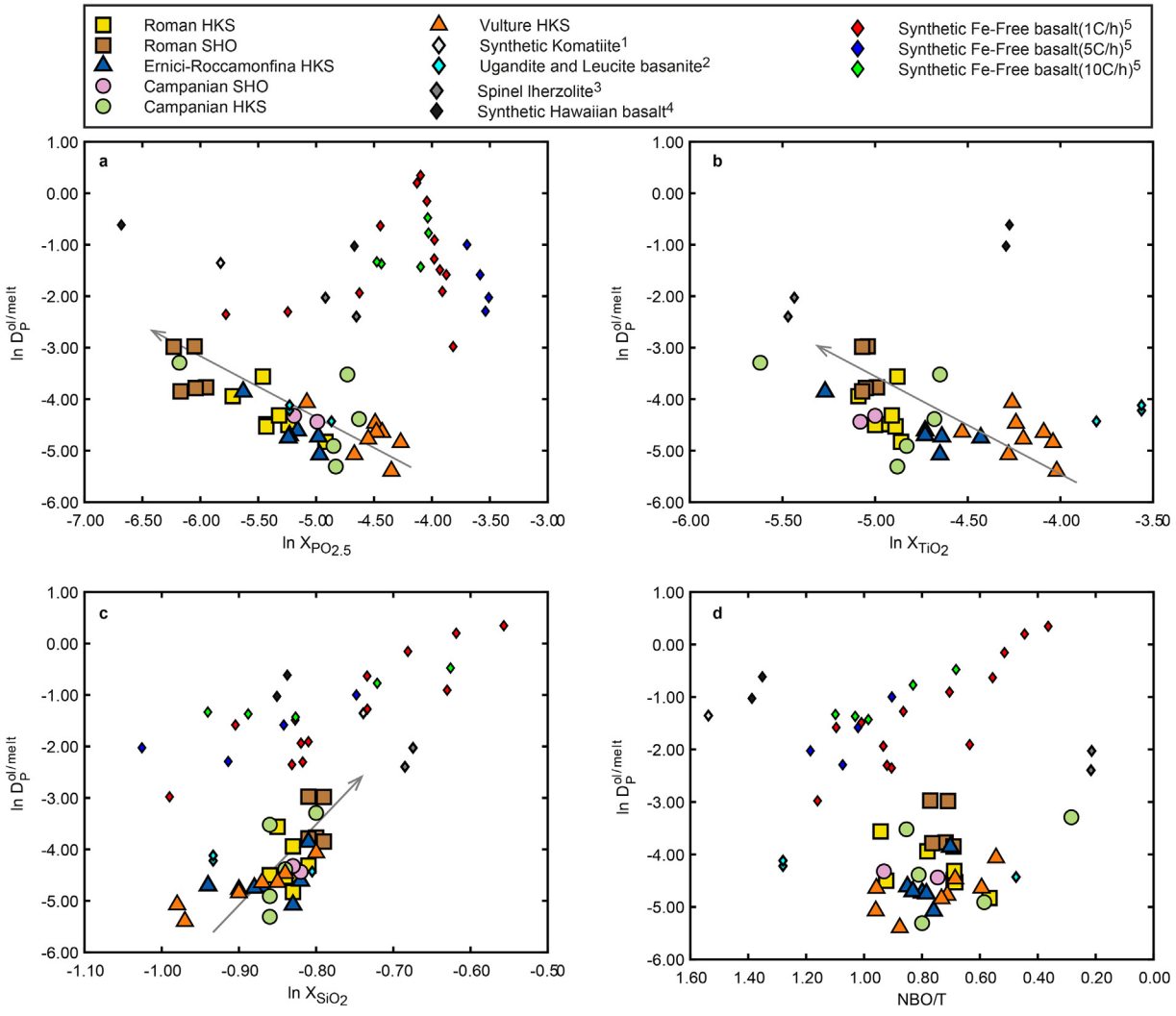

Fig. 8. Relationship between ln $D_P^{ol/melt}$ (a) and ln X_{SiO2}, (b) ln $X_{PO2.5}$, (c) ln X_{TiO2}, and NBO/T. Disregarding some data scatter, correlation of ln $D_P^{ol/melt}$ with ln X_{SiO2} and anticorrelation with ln $X_{PO2.5}$ and ln X_{TiO2} indicate that melt composition exerts a significant control on near-equilibrium partitioning of P into olivine. The negative correlation between mole fraction of P in the silicate melt ($X_{PO2.5}$) and ln $D_P^{ol/melt}$ suggests a deviation of P partitioning from Henry's law behaviour under (near) equilibrium conditions.

melt will result in a relative enrichment of P_2O_5. Early crystal fractionation thus predicts a negative correlation between the Fo contents of olivines and the P contents in the associated MI in the case of equilibrium partitioning. In addition, if crystal fractionation affects P incorporation into the olivine and crystallization proceeds under equilibrium conditions, the P contents of olivines in a given lava sample should be inversely correlated with their Fo contents, and P should increase from cores to rims in normally zoned olivine crystals. Instead, the olivines investigated in this study do not show these predicted trends (Figs. 2–4), neither within individual olivines nor at the population level. Although apatite occurs as an accessory phase in the groundmass of almost all samples studied, its saturation in the interval of early olivine crystallization is unlikely, as it is expected to appear very late in the crystallization sequence (Del Bello et al., 2014) or would require P_2O_5 concentrations in excess of 4 wt.% in the melt (Watson, 1980), which exceeds the contents in the MI analysed.

5.3.3. Growth rate

Relatively rapid crystal growth (Milman-Barris et al., 2008), fast cooling from high temperatures (Boesenberg et al., 2004; Boesenberg and Hewins, 2010), and diffusion-controlled, rapid dendritic olivine growth followed by slow overgrowth and infilling (Welsch et al., 2014) have been invoked as mechanisms for P enrichment in olivine. The rapid advance of a crystal face may result in local P enrichment in the boundary layer due to low volume diffusivities of P and Si in silicate melts (Spandler and O'Neill, 2010; Welsch et al., 2013; Watson et al., 2015), so that P ions unable to escape the advancing crystal face become trapped in the crystal lattice. In the case of solute trapping (Reitano et al., 1994), uptake by olivine will be controlled by the interplay between the diffusion rate of P in the melt and the growth rate of the advancing crystal face. Boundary layer enrichment, however, will not be limited to P, but must apply to all cations with similar diffusion rates and/or low partition coefficients that are rejected by the growing crystal. Hence, solute-trapping mechanism responsible for development of P-rich zones could also produce an enrichment of Al in the same zones since diffusivities of both elements are low in silicate melts as well as in olivine crystals (Spandler and O'Neill, 2010; Watson et al., 2015). The results from EPMA traverses in the investigated olivines clearly indicate that P zoning is either not accompanied by Al zoning, or is anticorrelated (e.g., Figs. 2 and 3). Therefore, unless the olivines investigated here underwent an extensive period of high temperature residency to relax Al zoning (dubious in view of the Fe-Mg re-equilibration patterns between host olivines and MIs), it is unlikely that the solute-trapping mechanism induced by high growth rate played a significant role in P uptake.

5.4. Phosphorous depletion zones around melt inclusions

Melt inclusions in the investigated olivines were virtually always surrounded by P-depleted zones (Figs. 2 and 3), as has also been observed elsewhere (McCanta et al., 2008; Milman-Barris et al., 2008; Ennis et al., 2010). Phosphorous depletion was generally associated with depletion in Cr and enrichment in Al. EPMA traverses showed that the decrease in the P concentration towards MI could be either gradual (profile 4 in Fig. 2c) or abrupt (profile 6 in Fig. 3b). In olivine phenocrysts with multiple MIs, the concentrations usually decrease gradually, starting at a more or less equal distances from the inclusions (Fig. 3b, profile 6). The depletion of P around MI resembles trends of re-equilibration between MI and host olivine. Post entrapment changes in MI include Fe-Mg exchange with host olivine or loss of volatiles (Danyushevsky et al., 2002a, 2002b). However, profiles and degree of P depletion around MI were often not identical and not related to the size or P_2O_5 content of MI, or to residence times inferred from Fe-loss (Danyushevsky et al., 2002b). This supports the hypothesis that diffusive exchange between MI and host olivine was minimal for P, consistent with its property as one of the most slowly diffusing cations in silicates (Watson et al., 2015).

Milman-Barris et al. (2008) considered the possibility that low-P zones around MI resulted from transcrystalline melt migration as described by Schiano et al. (2006), who observed that MI change from sub-spherical to a faceted, negative crystal shape during this process, and that host olivines lack any zoning after the melt had migrated. Considering that almost all MI investigated in this study were (sub-)spherical and that zoning in host olivines is widespread, transcrystalline melt migration is an unlikely mechanism to account for the low-P zones around MI in the Italian olivines.

Alternatively, the presence of P-poor zones can be the result of slow crystallization around MI walls (Milman-Barris et al., 2008). As a MI becomes gradually enclosed by the host crystal, supply of the main olivine constituents becomes limited, slowing down the crystallization of the MI walls. Since growth rate would be significantly reduced, incorporation of P into the olivine may become governed by equilibrium partitioning rather than kinetic or diffusion controlled. Boesenberg et al. (2004) and Boesenberg and Hewins (2010) showed experimentally that the melt-olivine equilibrium partition coefficient for P decreases with increasing duration of crystallization. This effect may thus explain the P depletion around MI. Aluminium enrichment around MI is consistent with such a supply-limited slow growth. As slow crystallization proceeds, the melt becomes enriched in Al and in other components that are rejected by the host olivine. The increased Al concentration resulted in Al-rich zones around MI, since as partitioning of Al between olivine and silicate melt deviates from Henry's law behaviour and D_{Al} increases with increasing activity of $AlO_{1.5}$ in the melt (Evans et al., 2008b). Consequently, we consider supply-limited slow crystallization against MI walls to be a plausible explanation for the formation of P-poor zones around the Italian MIs.

5.5. Phosphorous as indicator of magma chamber processes

Assimilation of carbonate wall rock is a well-documented process for Colli Albani HKS magmas (Peccerillo, 2005; Iacono Marziano et al., 2007; Gaeta et al., 2009), and has also been inferred for San Venanzo

KAM magma (Peccerillo, 2004; Nikogosian et al., 2013). In olivines from San Venanzo, crystallization from contaminated melts is manifested as development of P-enriched zones as shown in Fig. 9. The unzoned olivine interior, presumably crystallized from kamafugitic melt, is characterized by high Fo, low P and CaO contents whereas the area surrounding the melt embayment corresponds to a low Fo zone with elevated CaO and P contents. Virtually all elements exhibit diffusion profiles, which can either be explained by re-equilibration with a more evolved magma or by overgrowth from a melt compositionally modified by crustal assimilation. In contrast, the P profile indicates an abrupt event in the crystallization history presumably when overgrowth from the contaminated melt started (Fig. 9). The non-primary nature of the high-P, high-Ca olivines from Colli Albani is confirmed by exotic compositions of their MIs, which fall in the fields of melts and glasses with a carbonate assimilation signature (Iacono Marziano et al., 2007; Gaeta et al., 2009; Peccerillo et al., 2010; Nikogosian et al., 2013). As Fig. 10 shows, compositional differences exist in olivines in the samples from both centres, whereby those crystallized from contaminated melts are enriched in P and Ca, and have relatively low Fo contents. From these observations, it can be inferred that P in olivine, one of the least susceptible elements to post-crystallization changes such as diffusive re-equilibration/relaxation, is a sensitive tracer of sudden changes in melt composition associated with assimilation of wall rock at shallow crustal levels.

The sluggish diffusion of P and the sensitivity of uptake by olivines to melt composition and dynamics make P a versatile indicator of crystal-growth histories and magma processes in mafic systems. Among the many applications conceivable are identification of intricate mixing/interaction processes involving compositionally diverse magmas, or provision of a reliable immobile intra-crystal framework for calculations of phenocryst residence times from zoning patterns of diffusible cations.

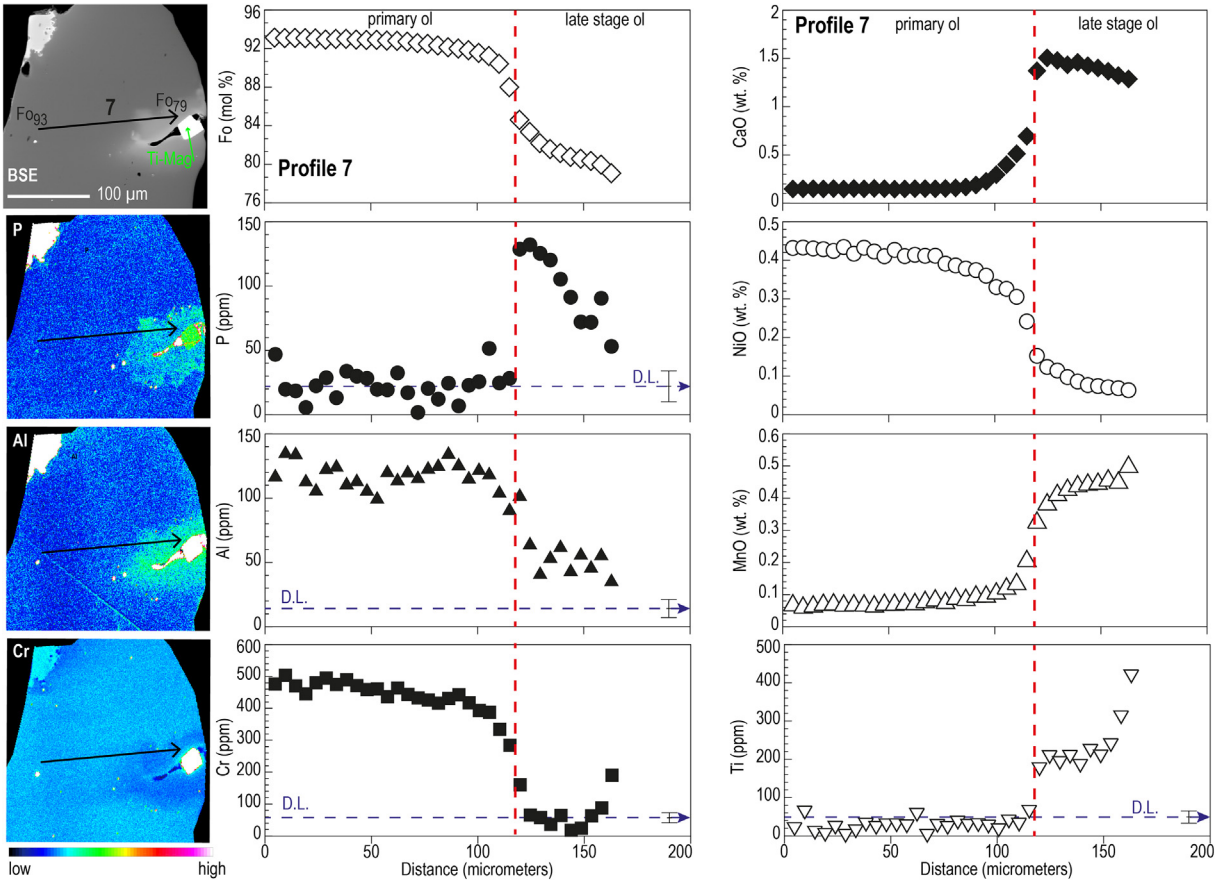

Fig. 9. Traverse between a high-Fo primary zone and an overgrowth zone produced by interaction with contaminated melt due to wall-rock assimilation in olivine SV 51. EPMA LOQ lines are plotted as blue dashed lines and labelled as D.L. in P, Ti, Cr plots to indicate where concentrations were lower than the LOQ. Boundary between the "primary core" and "overgrowth zone" is shown by the vertical red dashed line. Note that the P concentration is lower or near LOQ throughout the primary crystal core, and abruptly increases to around 130 ppm in the overgrowth zone, corresponding to elevated CaO and decreased Fo contents. The change in the P content is rather abrupt as opposed to more gradual changes in CaO and Fo contents resulting from diffusive re-equilibration between the primary core and the overgrowth. The sudden increase in the P content marks the beginning of the overgrowth zone. Traverse locations are shown in the backscatter electron (BSE) images. Error bars shown in the lower right corner of each diagram are two standard deviations based on counting statistics. Centre of the error bar corresponds to the detection limit for each element. Laser ablation craters (80 µm in diameter) are visible in each figure. Data for the profile are reported in Supplementary Table 3.

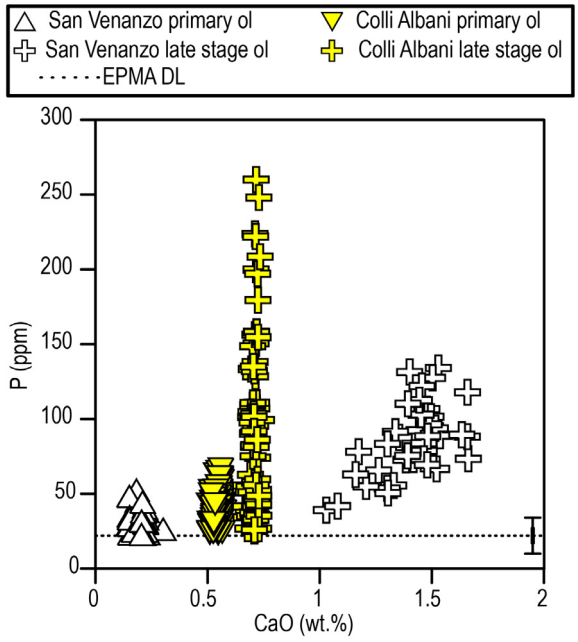

Fig. 10. Relationship between CaO and P contents of olivines from Colli Albani HKS and San Venanzo KAM samples based on EPMA traverses. Data for primary olivine cores are represented by normal and upside-down triangles and those for overgrowth/reaction zones by plus symbols. Both samples experienced interaction with melts contaminated by assimilation of carbonate rock (Peccerillo, 2004; Iacono Marziano et al., 2007; Gaeta et al., 2009; Peccerillo et al., 2010; Nikogosian et al., 2013). Primary cores of the Colli Albani HKS olivines have lower CaO contents than overgrowth or reaction zones, but the difference in P content is more pronounced. Primary cores of the San Venanzo KAM olivines are characterized by low CaO and P contents but overgrowth zones exhibit much higher CaO contents than the primary cores, as well as relatively high P contents.

6. SUMMARY

A systematic survey of olivine phenocrysts and their melt inclusions in mafic K-rich rocks from Quaternary volcanic centres across mainland Italy enabled us to identify relationships between P incorporation in early crystallizing olivines and melt composition for a range of calc-alkaline to kamafugitic rock types with variable degrees of K enrichment. In contrast to the overall high P contents of melts from which they crystallized (0.16–2.19 wt.% P_2O_5), the investigated set of olivines is marked by low concentrations (generally $\leq$ 200 ppm P, only occasionally up to 435 ppm) relative to those from subalkaline Hawaiian lavas and mantle olivines. Therefore, bulk P contents alone are not responsible for effective partitioning of P into olivine crystallizing from near-primary, mantle-derived magmas.

For the Italian magmatic systems, we infer that melt composition and crystallization dynamics stand out as discernible controls on the P uptake by olivine phenocrysts. The behaviour of P changes with overall melt composition, specifically X_{SiO2} and $X_{PO2.5}$, as apparent partition coefficients tend to increase with decreasing P_2O_5 activity. This influence of melt composition is in agreement with findings in experiments on synthetic K-free systems (Grant and Kohn, 2013). The asserted importance of crystal-growth kinetics (rapid versus slow growth), supposedly reflecting magma-evolution conditions, is consistent with the earlier finding for Hawaiian olivines that rapid growth largely controls P enrichments (Milman-Barris et al., 2008).

Phosphorous concentrations and zoning in the studied olivines are independent from compositional changes driven by crystal fractionation. Zoning patterns and concentrations of P are not correlated with Al, Cr, Li or Na in most of the Italian olivines. The melt inclusions are virtually always surrounded by P-poor zones that are also poor in Cr and enriched in Al and Ti. We attribute this phenomenon to supply-limited slow growth during entrapment of the melt. Our results for the heterogeneous group of Italian potassic systems highlights the apparent sensitivity of P incorporation by olivines to melt composition and crystallization dynamics, which, combined with its sluggish diffusion, make this element a versatile tracer of olivine-growth histories and underlying magma processes.

ACKNOWLEDGEMENTS

Pieter Vroon, Tilly Bouten, Sergei Matveev and Helen de Waard are thanked for assistance with XRF, LA-ICP-MS, and EPMA analyses. We thank Marc Norman for efficient editorial handling and Kendra J. Lynn and two anonymous reviewers for extensive, critical and constructive reviews. This research was funded by The Netherlands Research Centre for Integrated Solid Earth Science (ISES) through grant 6.2.12.

APPENDIX A. SUPPLEMENTARY MATERIAL

Supplementary data to this article can be found online at https://doi.org/10.1016/j.gca.2019.03.012.

REFERENCES

Adam J. and Green T. (2006) Trace element partitioning between mica- and amphibole-bearing garnet lherzolite and hydrous basanitic melt: 1. Experimental results and the investigation of controls on partitioning behaviour. *Contrib. to Mineral. Petrol.* **152**, 1–17.

Anderson A. T. and Greenland L. P. (1969) Phosphorus fractionation diagram as a quantitative indicator of crystallization differentiation of basaltic liquids. *Geochim. Cosmochim. Acta* **33**, 493–505.

Batanova V. G., Sobolev A. V. and Kuzmin D. V. (2015) Trace element analysis of olivine: high precision analytical method for JEOL JXA-8230 electron probe microanalyser. *Chem. Geol.* **419**, 149–157.

Baziotis I., Asimow P. D., Ntaflos T., Boyce J. W., McCubbin F. M., Koroneos A., Perugini D., Flude S., Storey M., Liu Y. S., Klemme S. and Berndt J. (2017) Phosphorus zoning as a recorder of crystal growth kinetics: application to second-generation olivine in mantle xenoliths from the Cima Volcanic Field. *Contrib. Mineral. Petrol.* **172**.

Del Bello E., Mollo S., Scarlato P., von Quadt A., Forni F. and Bachmann O. (2014) New petrological constraints on the last eruptive phase of the Sabatini Volcanic District (central Italy): clues from mineralogy, geochemistry, and Sr-Nd isotopes. *Lithos* **205**, 28–38.

De Hoog J. C. M., Mason P. R. D. and van Bergen M. J. (2001) Sulfur and chalcophile elements in subduction zones: constraints from a laser ablation ICP-MS study of melt inclusions from Galunggung Volcano. *Indonesia. Geochim Cosmochim Acta* **65**, 3147–3164.

Boesenberg J., Ebel D. S. and Hewins R. (2004) An experimental study of phosphoran olivine and its significance in main group pallasites. In *Lunar and Planetary Science XXXV*, p. 1366.

Boesenberg J. S. and Hewins R. H. (2010) An experimental investigation into the metastable formation of phosphoran olivine and pyroxene. *Geochim. Cosmochim. Acta* **74**, 1923–1941.

Brunet F. and Chazot G. (2001) Partitioning of phosphorus between olivine, clinopyroxene and silicate glass in an spinel lherzolite xenolith from Yemen. *Chem. Geol.* **176**, 51–72.

Canil D., Schulze D. J., Hall D., Hearn, Jr., B. C. and Milliken S. M. (2003) Lithospheric roots beneath western Laurentia: the geochemical signal in mantle garnets. *Can. J. Earth Sci.* **40**, 1027–1051.

Chakraborty S. (2010) Diffusion coefficients in olivine, wadsleyite and ringwoodite. *Rev. Mineral Geochemistry* **72**, 603–639.

Conticelli S., Laurenzi M. A., Giordano G., Mattei M., Avanzinelli R., Melluso L., Tommasini S., Boari E., Cifelli F. and Perini G. (2010) Leucite-bearing (kamafugitic/leucititic) and –free (lamproitic) ultrapotassic rocks and associated shoshonites from Italy: constraints on petrogenesis and geodynamics. *J. Virtual Explor.* **36**, paper 20.

Conticelli S. and Peccerillo A. (1989) Petrological significance of high-pressure ultramafic xenoliths from ultrapotassic rocks of Central Italy. *Lithos* **24**, 305–322.

Coogan L. A., Hain A., Stahl S. and Chakraborty S. (2005) Experimental determination of the diffusion coefficient for calcium in olivine between 900°C and 1500°C. *Geochim. Cosmochim. Acta* **69**, 3683–3694.

Danyushevsky L. V., McNeill A. W. and Sobolev A. V. (2002a) Experimental and petrological studies of melt inclusions in phenocrysts from mantle-derived magmas: an overview of techniques, advantages and complications. *Chem. Geol.* **183**, 5–24.

Danyushevsky L. V., Sokolov S. and Falloon T. J. (2002b) Melt inclusions in olivine phenocrysts: using diffusive re-equilibration to determine the cooling history of a crystal, with implications for the origin of olivine-phyric volcanic rocks. *J. Petrol.* **43**, 1651–1671.

De Hoog J. C. M., Gall L. and Cornell D. H. (2010) Trace-element geochemistry of mantle olivine and application to mantle petrogenesis and geothermobarometry. *Chem. Geol.* **270**, 196–215.

Dohmen R., Becker H.-W. and Chakraborty S. (2007) Fe–Mg diffusion in olivine I: experimental determination between 700 and 1,200°C as a function of composition, crystal orientation and oxygen fugacity. *Phys. Chem. Miner.* **34**, 389–407.

Ennis M. E., McSween H. Y., Patchen A. and Taylor L. A. (2010) Zoning of phosphorus within the olivines of the olivine-phyric shergottite Dhofar 019. In *Lunar and Planetary Science XXXXI*, p. 2404.

Evans T. M., Hugh H. S. and Tuff J. (2008a) The influence of melt composition on the partitioning of REEs, Y, Sc, Zr and Al between forsterite and melt in the system CMAS. *Geochim. Cosmochim. Acta* **72**, 5708–5721.

Evans T. M., Neill H. S. C. O. and Tuff J. (2008b) The influence of melt composition on the partitioning of REEs, Y, Sc, Zr and Al between forsterite and melt in the system CMAS. *Geochim. Cosmochim. Acta* **72**, 5708–5721.

Foley S. F., Jacob D. E. and O'Neill H. S. C. (2011) Trace element variations in olivine phenocrysts from Ugandan potassic rocks as clues to the chemical characteristics of parental magmas. *Contrib. to Mineral. Petrol.* **162**, 1–20.

Foley S. F., Prelevic D., Rehfeldt T. and Jacob D. E. (2013) Minor and trace elements in olivines as probes into early igneous and mantle melting processes. *Earth Planet. Sci. Lett.* **363**, 181–191.

Gaeta M., Di Rocco T. and Freda C. (2009) Carbonate assimilation in open magmatic systems: the role of melt-bearing skarns and cumulate-forming processes. *J. Petrol.* **50**, 361–385.

Grant T. B. and Kohn S. C. (2013) Phosphorus partitioning between olivine and melt: an experimental study in the system Mg2SiO4-Ca2Al2Si2O9-NaAlSi3O8-Mg3(PO4)2. *Am. Mineral.* **98**, 1860–1869.

Gurenko A. A., Hoernle K. A., Sobolev A. V., Hauff F. and Schmincke H. U. (2010) Source components of the Gran Canaria (Canary Islands) shield stage magmas: evidence from olivine composition and Sr-Nd-Pb isotopes. *Contrib. Mineral. Petrol.* **159**, 689–702.

Hofmann A. E. (2010) *Micron- to Sub-Micron-Scale Trace Element Zonations in Zircon and Olivine* Ph.D. thesis. California Institute Of Technology.

Iacono Marziano G., Gaillard F. and Pichavant M. (2007) Limestone assimilation and the origin of CO2 emissions at the Alban Hills (Central Italy): constraints from experimental petrology. *J. Volcanol. Geotherm. Res.* **166**, 91–105.

Jarosewich E., Nelen J. A. and Norberg J. A. (1980) Reference samples for electron microprobe analysis. *Geostand. Newsl.* **4**, 43–47.

Jochum K. P., Stoll B., Herwig K., Willbold M., Hofmann A. W., Amini M., Aarburg S., Abouchami W., Hellebrand E., Mocek B., Raczek I., Stracke A., Alard O., Bouman C., Becker S., Dücking M., Brätz H., Klemd R., de Bruin D., Canil D., Cornell D., de Hoog C.-J., Dalpé C., Danyushevsky L., Eisenhauer A., Gao Y., Snow J. E., Groschopf N., Günther D., Latkoczy C., Guillong M., Hauri E. H., Höfer H. E., Lahaye Y., Horz K., Jacob D. E., Kasemann S. A., Kent A. J. R., Ludwig T., Zack T., Mason P. R. D., Meixner A., Rosner M., Misawa K., Nash B. P., Pfänder J., Premo W. R., Sun W. D., Tiepolo M., Vannucci R., Vennemann T., Wayne D. and Woodhead J. D. (2006) MPI-DING reference glasses for in situ microanalysis: new reference values for element concentrations and isotope ratios. *Geochem. Geophys. Geosyst.* **7**.

Jollands M. C., Hermann J., St. O'Neill H. C., Spandler C. and Padrón-Navarta J. A. (2016) Diffusion of Ti and some divalent cations in olivine as a function of temperature, oxygen fugacity, chemical potentials and crystal orientation. *J. Petrol.* **57**, 1983–2010.

Jollands M. C., O'Neill H. S. C., Van Orman J., Berry A. J., Hermann J., Newville M. and Lanzirotti A. (2018) Substitution and diffusion of Cr2+and Cr3+in synthetic forsterite and natural olivine at 1200–1500 °C and 1 bar. *Geochim. Cosmochim. Acta* **220**, 407–428.

Kamenetsky V., Métrich N. and Cioni R. (1995) Potassic primary melts of vulsini (Roman Province): evidence from mineralogy and melt inclusions. *Contrib. Mineral. Petrol.* **120**, 186–196.

Li Y., Zhang A.-C., Chen J.-N., Gu L.-X. and Wang R.-C. (2017) Formation of phosphorus-rich olivine in Dar al Gani 978 carbonaceous chondrite through fluid-assisted metamorphism. *Am. Mineral.* **102**, 98–107.

Le Maitre R. W., Streckeisen A., Zanettin B., Le Bas M. J., Bonin B. and Bateman P. (2002) Classification and nomenclature. In *Igneous Rocks: A Classification and Glossary of Terms* (eds. R. W. Le Maitre, A. Streckeisen, B. Zanettin, M. J. Le Bas, B. Bonin and P. Bateman). Cambridge University Press, Cambridge, pp. 3–42.

Mallmann G. and O'Neill H. S. C. (2009) The crystal/melt partitioning of V during mantle melting as a function of

oxygen fugacity compared with some other elements (Al, P, Ca, Sc, Ti, Cr, Fe, Ga, Y, Zr and Nb). *J. Petrol.* **50**, 1765–1794.

Mallmann G., O'Neill H. S. C. and Klemme S. (2009) Heterogeneous distribution of phosphorus in olivine from otherwise well-equilibrated spinel peridotite xenoliths and its implications for the mantle geochemistry of lithium. *Contrib. Mineral. Petrol.* **158**, 485–504.

McCanta M. C., Beckett J. R. and Stolper E. M. (2016) Correlations and zoning patterns of phosphorus and chromium in olivine from H chondrites and the LL chondrite Semarkona. *Meteorit. Planet. Sci.* **51**, 520–546.

McCanta M. C., Beckett J. R. and Stolper E. M. (2008) Phosphorus zonation as a record of olivine crystallization history. In *Goldschmidt Conference Abstracts 2008*, p. 610.

McCanta M. C., Beckett J. R. and Stolper E. M., Phosphorus Zonation in H Chondrite Olivines: The Effects of Increasing Petrologic Grade, In: Lunar and Planetary Science XXXX, 2009, 2048.

Milman-Barris M. S., Beckett J. R., Baker M. B., Hofmann A. E., Morgan Z., Crowley M. R., Vielzeuf D. and Stolper E. (2008) Zoning of phosphorus in igneous olivine. *Contrib. Mineral. Petrol.* **155**, 739–765.

Mysen B. O. and Richet P. (2005) *Silicate Glasses and Melts: Properties and Structure*. Elsevier.

Nikogosian I. K., Elliott T. and Touret J. L. R. (2002) Melt evolution beneath thick lithosphere: a magmatic inclusion study of La Palma. *Canary Islands. Chem. Geol.* **183**, 169–193.

Nikogosian I., Ersoy Ö., Whitehouse M., Mason P. R. D., de Hoog J. C. M., Wortel R. and van Bergen M. J. (2016) Multiple subduction imprints in the mantle below Italy detected in a single lava flow. *Earth Planet. Sci. Lett.* **449**, 12–19.

Nikogosian I. K. and van Bergen M. J. (2010) Heterogeneous mantle sources of potassium-rich magmas in central-southern Italy: Melt inclusion evidence from Roccamonfina and Ernici (Mid Latina Valley). *J. Volcanol. Geotherm. Res.* **197**, 279–302.

Nikogosian I. K., van Bergen M. J. and Chaneva S. (2013) Multiple origins of carbon in italian kamafugite melt. *Mineral. Mag.* **77**, 1851.

Nikogosian I. and Sobolev A. (1997) Ion-microprobe analysis of melt Inclusions in olivine: experience in estimating the olivine-melt partition coefficients of trace elements. *Geochem. Int.* **35**, 119–126.

O'Neill H. S. C. and Eggins S. M. (2002) The effect of melt composition on trace element partitioning: an experimental investigation of the activity coefficients of FeO, NiO, CoO, MoO2 and MoO3 in silicate melts. *Chem. Geol.* **186**, 151–181.

O'Neill H. S. C. and Mavrogenes J. A. (2002) The sulfide capacity and the sulfur content at sulfide saturation of silicate melts at 1400degreesC and 1 bar. *J. Petrol.* **43**, 1049–1087.

Pearce N. J. G., Perkins W. T., Westgate J. A., Gorton M. P., Jackson S. E., Neal C. R. and Chenery S. P. (1997) A Compilation of new and published major and trace element Data for NIST SRM 610 and NIST SRM 612 glass reference materials. *Geostand. Geoanal. Res.* **21**, 115–144.

Peccerillo A. (2004) Carbonate-rich pyroclastic rocks from central Apennines: carbonatites or carbonated rocks? A commentary. *Period. Min.* **73**, 165–175.

Peccerillo A. (2017) *Cenozoic Volcanism in the Tyrrhenian Sea Region*, second ed. Springer International Publishing.

Peccerillo A. (2005) *Plio-Quaternary Volcanism in Italy*, first ed. Springer-Verlag.

Peccerillo A., Federico M., Barbieri M., Brilli M. and Wu T.-W. (2010) Interaction between ultrapotassic magmas and carbonate rocks: Evidence from geochemical and isotopic (Sr, Nd, O) compositions of granular lithic clasts from the Alban Hills Volcano, Central Italy. *Geochim. Cosmochim. Acta* **74**, 2999–3022.

Reitano R., Smith P. M. and Aziz M. J. (1994) Solute trapping of group III, IV, and V elements in silicon by an aperiodic stepwise growth mechanism. *J. Appl. Phys.* **76**, 1518–1529.

Sanfilippo A., Tribuzio R. and Tiepolo M. (2014) Mantle-crust interactions in the oceanic lithosphere: constraints from minor and trace elements in olivine. *Geochim. Cosmochim. Acta* **141**, 423–439.

Schiano P., Provost A., Clocchiatti R. and Faure F. (2006) Transcrystalline melt migration and earth's mantle. *Science* **80** (314), 970–974.

Shea T., Lynn K. J. and Garcia M. O. (2015) Cracking the olivine zoning code: Distinguishing between crystal growth and diffusion. *Geology* **43**, 935–938.

Sobolev A.V., Dmitriev L.V., Barsukov V.N., Nevsorov V.N., Slutsky A.B., The formation conditions of high magnesium olivines from the monomineral fraction of luna-24 regolith. Lunar Planet. Sci. Conf. 1980, 105–106.

Sobolev A. V., Hofmann A. W., Kuzmin D. V., Yaxley G. M., Arndt N. T., Chung S.-L., Danyushevsky L. V., Elliott T., Frey F. A., Garcia M. O., Gurenko A. A., Kamenetsky V. S., Kerr A. C., Krivolutskaya N. A., Matvienkov V. V., Nikogosian I. K., Rocholl A., Sigurdsson I. A., Sushchevskaya N. M. and Teklay M. (2007) The amount of recycled crust in sources of mantle-derived melts. *Science* **316**, 412–417.

Spandler C. and O'Neill H. S. C. (2010) Diffusion and partition coefficients of minor and trace elements in San Carlos olivine at 1,300°C with some geochemical implications. *Contrib. Mineral. Petrol.* **159**, 1–28.

Spandler C., O'Neill H. S. C. and Kamenetsky V. S. (2007) Survival times of anomalous melt inclusions from element diffusion in olivine and chromite. *Nature* **447**, 303–306.

Toplis M. J., Libourel G. and Carroll M. R. (1994) The role of phos- phorus in crystallization processes of basalt: an experimental study. *Geochim. Cosmochim. Acta* **58**, 797–810.

Watson E. B. (1980) Apatite and phosphorus in mantle source regions: an experimental study of apatite/melt equilibria at pressures to 25 kbar. *Earth Planet. Sci. Lett.* **51**, 322–335.

Watson E. B., Cherniak D. J. and Holycross M. E. (2015) Diffusion of phosphorus in olivine and molten basalt. *Am. Mineral.* **100**, 2053–2065.

Welsch B., Faure F., Famin V., Baronnet A. and Bachèlery P. (2013) Dendritic crystallization: a single process for all the textures of olivine in basalts? *J. Petrol.* **54**, 539–574.

Welsch B., Hammer J. and Hellebrand E. (2014) Phosphorus zoning reveals dendritic architecture of olivine. *Geology* **42**, 867–870.

Witt-Eickschen G. and O'Neill H. S. C. (2005) The effect of temperature on the equilibrium distribution of trace elements between clinopyroxene, orthopyroxene, olivine and spinel in upper mantle peridotite. *Chem. Geol.* **221**, 65–101.

Xing C. M., Wang C. Y. and Tan W. (2017) Disequilibrium growth of olivine in mafic magmas revealed by phosphorus zoning patterns of olivine from mafic–ultramafic intrusions. *Earth Planet. Sci. Lett.* **479**, 108–119.

Associate editor: Jeffrey G. Catalano